

1 **Petroleum evolution within the Tarim Basin, NW China: Insights from organic**  
2 **geochemistry, fluid inclusions, and Re-Os geochronology of the Halahatang Oilfield**

3  
4 Xiang Ge<sup>1,2</sup>, Chuanbo Shen<sup>1\*</sup>, David Selby<sup>2,5</sup>, Martin Feely<sup>3</sup>, Guangyou Zhu<sup>4</sup>

5  
6 <sup>1</sup>Key Laboratory of Tectonics and Petroleum Resources (China University of  
7 Geosciences), Ministry of Education, Wuhan, 430074, China

8 <sup>2</sup>Department of Earth Sciences, Durham University, Durham, DH1 3LE, UK

9 <sup>3</sup>Earth and Ocean Sciences, School of Natural Sciences, National University of Ireland,  
10 Galway, Ireland

11 <sup>4</sup>Research Institute of Petroleum Exploration and Development, PetroChina, Beijing  
12 100083, China

13 <sup>5</sup>State Key Laboratory of Geological Processes and Mineral Resources, School of Earth  
14 Resources, China University of Geosciences, Wuhan, 430074, China

15  
16 **\*Corresponding author E-mail: [cugshen@126.com](mailto:cugshen@126.com)**

17  
18 **Acknowledgements**

19 This work was supported by the National Natural Science Foundation of China (No.  
20 41802168, 41672140, 41372140), the PetroChina Innovation Foundation (No. 2016D-  
21 5007-0103), the Program of Introducing Talents of Discipline to Universities (No.  
22 B14031), the Outstanding Youth Funding of Natural Science Foundation of Hubei  
23 Province (No. 2016CFA055), and the Fundamental Research Fund for the Central  
24 Universities, China University of Geosciences (Wuhan, No. CUG180617, CUGCJ1820,  
25 CUGCJ1712), and Open Topic Fund from Key Laboratory of Tectonics and Petroleum  
26 Resources of Ministry of Education (TPR-2018-11). We thank Dr. Emmanuel Laverret of  
27 CV Associés Engineering, France for the fluid inclusion analysis and PVTx modelling.

28 DS acknowledges the Total Endowment Fund and the Dida Scholarship from CUG  
29 Wuhan. Xiang Ge was supported by a postgraduate award from the China Scholarship  
30 Council (CSC). We acknowledge the analytical support of Antonia Hofmann, Geoff  
31 Nowell and Chris Ottley. Lastly, we thank Barry J. Katz, Ling Gao and two anonymous  
32 reviewers for their constructive reviews which helped improve the paper.

33

34 **Abstract**

35 The newly discovered Halahatang oilfield in the northern Tarim Basin has a potential  
36 resource of > 70 Bbbls of oil. Oil organic geochemical data from the Halahatang oilfield  
37 indicate that the oils are of moderate maturity, biodegraded, and represent one oil family,  
38 derived from the same Paleozoic marine source. Modeling of coeval aqueous and  
39 hydrocarbon-bearing inclusion data provide fluid trapping temperatures and pressures of  
40 100 to 110 °C and ~39 to 59 MPa, respectively. The fluid inclusion data coupled with the  
41 previous basin model studies, suggests a single prolonged oil migration event during the  
42 Permian. Rhenium-Osmium (Re-Os) isotope data oil yield an Early Permian Re-Os age  
43 of  $285 \pm 48$  Ma. The age agrees with the timing of maturation of the Paleozoic source via  
44 burial history modelling but is slightly older (~5 - 55 myr) than the oil  
45 migration/accumulation timing implied by the basin modelling coupled with fluid  
46 inclusion analysis and the published reservoir illite K-Ar dates. Thus, the oil Re-Os date  
47 suggests that oil generation in the Halahatang Depression of the Tarim Basin occurred  
48 during the Early Permian, rather than the Silurian as previously proposed, with  
49 subsequent oil migration/accumulation occurring during the Mid-Late Permian as  
50 recorded by basin modelling, coupled with fluid inclusion analysis and illite K-Ar dating.  
51 In addition to promoting petroleum exploration in the Tarim Basin, this study that  
52 combines crude oil Re-Os isotope dating and traditional analytical methods (organic  
53 geochemistry/fluid inclusion analysis) to constrain petroleum evolution is applicable to  
54 hydrocarbon systems worldwide.

55

56

57 **Keywords**

58 Petroleum evolution; Re-Os geochronology; Organic geochemistry; Fluid inclusions;  
59 Halahatang oilfield; Tarim Basin

60

61 **1 Introduction**

62 The accurate key timing of petroleum evolution (e.g., oil generation, migration /  
63 accumulation) is vital to understand the evolution of a petroleum system (Liu et al., 2013;  
64 Qiu et al., 2011), and is crucial for hydrocarbon exploration in a target region (Roberts et  
65 al., 2004). Although thousands of oilfields are known worldwide, understanding how to  
66 precisely constrain the key events of a petroleum system remains challenging (Liu et al.,  
67 2013; Mark et al., 2010; Roberts et al., 2004). Aimed at solving these problems, the  
68 oilfield in Tarim Basin, northwest China was selected as an example in this study. The  
69 Tarim basin is bordered by the Tian Shan, West Kunlun and A'erjin orogenic belts to the  
70 north, southwest, and southeast, respectively (Lin et al., 2015; Zhang et al., 2007a) (Fig.  
71 1B). The basin encompasses an area of 560,000 km<sup>2</sup> (~216,217 mi<sup>2</sup>) and contains up to  
72 ~14 km (~8.7 mi) of sedimentary strata. It has had a complex tectonic evolution (e.g.,  
73 Caledonian, Hercynian, Indosinian-Yanshan and Himalayan orogenies). The basin  
74 contains significant petroleum potential (more than 70 billion barrels oil (Bbbls) and 250  
75 trillion cubic feet (Tcf) of gas) (Lin et al., 2015; Xiao and Tang, 2003; Xu et al., 2004).  
76 The Tarim Basin is the largest known onshore petroliferous basin in China, with only an  
77 estimated 10 percent of the total potential reserves presently discovered (Li, 2009; Xu et  
78 al., 2004). Although the Tarim Basin is considered to contain the most important future  
79 oil and gas resources in China (Li, 2009), the multiple tectonic events that the basin

80 records have led to a complex hydrocarbon evolution, which has hampered oil and gas  
81 exploration (Li, 2009; Lin et al., 2015; Zhang et al., 2007a).

82 More than thirty oil fields (e.g., Dawanqi, Lunnan, Tahe, Tazhong, Hetian and Bashituo)  
83 have been discovered throughout the Tarim Basin during the past three decades (Xu et al.,  
84 2004; Zhao et al., 2004). More recently discovered is the deeply buried (>6000 m)  
85 (>19,685 ft) Early Paleozoic carbonate Yijianfang Formation in the Halahatang  
86 depression of the northern Tarim Basin that has a current estimated reserve of >4 Bbbls of  
87 oil (Zhu et al., 2013a), which supports the reported resource potential within the Tarim  
88 Basin (Li, 2009; Xu et al., 2004). However, both the source and timing of hydrocarbon  
89 generation and accumulation in the Tarim Basin remain debated (Chang et al., 2013a; Li,  
90 2009; Li et al., 2010; Liao et al., 2010; Tian, 2005; Xiao et al., 2012). Hydrocarbon  
91 maturation models propose that the Neoproterozoic and Early Cambrian shales are the  
92 main source for the Shaya Uplift oilfield in the northern Tarim Basin (Li, 2009) and the  
93 Late Cambrian to Ordovician shales are the suggested oil source in Kongquehe area in  
94 northeast Tarim Basin (Tian, 2005). Based on both biomarker and  $\delta^{13}\text{C}$  analysis of  
95 individual *n*-alkanes for oils, a mixed origin (Cambrian–Lower Ordovician and Middle-  
96 Upper Ordovician) has been proposed for the central Tarim Basin (Li et al., 2010). Basin  
97 modeling in the Caohu Depression in the northern Tarim Basin considers the Early  
98 Ordovician (ca. 400 Ma) to be a key time of oil generation and migration (Tian, 2005).  
99 This is, in part, supported by authigenic illite K-Ar dating (ca. 380 Ma) from the Late  
100 Silurian sandstone reservoir in the central Tarim Basin (Zhang et al., 2004). However,  
101 younger migration ages are also proposed in the central and northern Tarim Basin by  
102 authigenic illite K-Ar dates of ca. 250 and ca. 20 Ma (Zhang et al., 2004; Zhu et al.,

103 2013c).

104 In the newly discovered Halahatang oil field, previous GC-MS (terpane and sterane  
105 characteristics) analysis on the oil and potential source rocks invoke both the shales of the  
106 Cambrian Yuertusi Formation, as well as Middle-Late Ordovician carbonates of the  
107 Lianglitage and Sangtamu Formations as the main sources of the petroleum (Chang et al.,  
108 2013a; Lu et al., 2008; Xiao et al., 2016; Zhu et al., 2013a). The current burial history  
109 models and fluid inclusion data propose several age models for the petroleum evolution  
110 in the Halahatang oil field (e.g., Late Silurian, Late Permian and Neogene) (Chang et al.,  
111 2013a; Si, 2013; Xiao et al., 2012; Zhu et al., 2013a). As a result the following key  
112 aspects of the petroleum systems are debated: (1) the source(s) of the oil; (2) the timing  
113 of oil generation, and (3) the timing of oil charging within the Tarim Basin.

114 Rhenium-osmium (Re-Os) isotope analysis on hydrocarbons has shown potential to  
115 determine the absolute timing of hydrocarbon generation (Cumming et al., 2014; Finlay  
116 et al., 2011; Ge et al., 2016; Ge et al., 2018a; Ge et al., 2018b; Georgiev et al., 2016;  
117 Lillis and Selby, 2013; Selby and Creaser, 2005; Selby et al., 2007). Further, authigenic  
118 illite K-Ar (Ar-Ar) dating from the oil reservoir and fluid inclusion studies can help  
119 record the timing of oil migration and reservoir filling (Guo et al., 2012; Hamilton et al.,  
120 1989; Lee et al., 1985; Mark et al., 2010; Zhang et al., 2004). In this study, we apply and  
121 discuss new oil geochemical analysis, fluid inclusion analysis, and Re-Os geochronology  
122 along with previous published sandstone authigenic illite K-Ar dating (Zhang and Luo,  
123 2011; Zhu et al., 2012), to quantitatively determine the petroleum evolution (timing of oil  
124 generation, migration/accumulation) associated with the Halahatang oilfield of the  
125 northern Tarim Basin. In addition, this work demonstrate this combined approach can

126 yield quantitative data to establish the timing for petroleum evolution that may aid in the  
127 further understanding of both the temporal and spatial evolution of hydrocarbon systems  
128 worldwide.

129

## 130 **2 Geological setting**

131 The Halahatang depression occupies an area of ~40,000 km<sup>2</sup> (15,444 mi<sup>2</sup>) within the  
132 centre of the Tabei Uplift in the northern Tarim Basin (Zhu et al., 2011). The Halahatang  
133 depression is bordered by the Yingmaili, Luntai, and Lunnan Uplift to the west, north and  
134 east, respectively, and the North Depression to the south (Fig. 1C). The geology of the  
135 Halahatang depression is characterized by a thick sequence of Cambrian to Quaternary  
136 strata (~14 km) (~8.7 mi) (Fig. 2) (Jia and Wei, 2002; Zhang and Huang, 2005). The  
137 Cambrian to Ordovician strata (~4.5 km) (~2.8 mi) comprise shallow marine to lagoonal  
138 carbonates (Jia and Wei, 2002), with the Silurian to Devonian strata being represented by  
139 ~1 km (~0.62 mi) of fine-grained red beds and sandstones (Zhang and Huang, 2005), and  
140 the Carboniferous to Permian section is characterized by a ~1 km (~0.62 mi) thick  
141 interval of sandstone and mudstone (Chang et al., 2013b). Since the Triassic the renewed  
142 subsidence of the Halahatang depression has led to the accumulation of ~6 km (3.73 mi)  
143 of Mesozoic to Cenozoic fluvio-lacustrine sediments (Zhang and Huang, 2005).

144 The Halahatang depression records multiple tectonic events. The Late Ordovician  
145 Caledonian Orogeny resulted in the uplift of the northern and central parts of the Tarim  
146 Basin (Zhang et al., 2007a). The region encompassing the Halahatang depression existed  
147 as a marginal foreland basin until the Late Permian (Jia and Wei, 2002; Wei et al., 2000;  
148 Zhu et al., 2011), and suffered uplift during the Hercynian Orogeny (Jia and Wei, 2002).

149 Since the Triassic the Halahatang depression experienced several burial and uplift events  
150 controlled by the closure of the Tethys Ocean and collision between Indian and Eurasian  
151 Plates (Yanshan and Himalayan orogenies) (Jia and Wei, 2002; Xu et al., 2016; Zhang  
152 and Huang, 2005; Zhu et al., 2011).

153 In the Halahatang depression, the carbonates of the Middle Ordovician Yijianfang  
154 Formation (>6,000 m deep) (>19,685 ft deep) is the main hydrocarbon reservoir, with  
155 Silurian and Triassic sandstones also considered as potential reservoir units (Zhu et al.,  
156 2013a) (Fig. 2). The source rock for the oil is still debated, but the main sources are  
157 considered to be the shales of the Cambrian Yuertusi Formation, and organic-rich  
158 carbonates of the Middle to Late Ordovician Lianglitage and Sangtamu formations  
159 (Chang et al., 2013b; Cui et al., 2009; Huo et al., 2016; Xiao et al., 2016). The dense  
160 shale or mudstone above the reservoirs are considered the cap rocks (Zhang and Huang,  
161 2005; Zhu et al., 2013a).

162

### 163 **3 Samples and methods**

164 Five oil samples from separate wells (Ha9, Ha11, Ha15-2, Ha701 and XK4-3) in the  
165 Halahatang depression were collected for GC-MS and Re-Os analysis (Fig. 1C). All the  
166 oil samples are from the Middle Ordovician Yijianfang Formation between ~6550m  
167 (21,489 ft) and 6850 m (22,474 ft) (Table 1). The oil physical property and organic  
168 compositions were collected from the unpublished reports of the Tarim Oil and Gas  
169 Company. The experiments were conducted at Research Institute of Petroleum  
170 Exploration and Development, PetroChina, Beijing with the oil density, oil viscosity and  
171 oil fractions measured following three different national standard methods (General

172 Administration of Quality Supervision Inspection and Quarantine of the People's  
173 Republic of China, 2011; National Development and Reform Commission, 2008;  
174 National Energy Administration of the People's Republic of China, 1993). The oil  
175 density, viscosity, and API values are 0.83 - 0.10, 3.15 - 342.3, and 8.46 - 38.37,  
176 respectively. The organic compositions, wax, sulfur, saturate, aromatic, resin, and  
177 asphaltene of the oil are ~6.0 %, ~0.6 %, ~56.1 %, ~16.5 %, ~4.7 %, and ~18.7 %,   
178 respectively. All the oil samples, with the exception of the oil from Well Ha701, are  
179 characterized by low viscosity (<0.90), a high API value (>29), and low asphaltene  
180 content (<25 %) (Table 1). Thus all the oils are characterized as light crude oil. However,  
181 the oil from well Ha701 possesses a high viscosity (~342) and asphaltene content  
182 (~34 %) and low API value (8.46) (Table 1), which characterizes the oil as heavy oil  
183 (Schenk et al., 2006; Zhang et al., 1990).

184 The gas chromatography mass spectrometry (GC-MS) analysis of the oil samples were  
185 conducted at the China University of Geoscience (Wuhan) following the analytical  
186 procedure of (Zhang et al., 2015). Approximately 30 mg of crude oil sample was  
187 dissolved in 50 ml of *n*-hexane and left for 12 hrs at room temperature. The solution was  
188 then filtered, with all the filtrates collected and evaporated under nitrogen gas to 0.5 ml.  
189 A chromatographic column (30 cm × 10 mm in diameter) was prepared using a mixed  
190 stationary phase of activated silica gel and alumina with a ratio of 3:2 (Yang et al., 2009).  
191 The concentrated sample was transferred to the chromatographic column for further  
192 separation. The saturated hydrocarbon fraction was eluted with *n*-hexane (25 ml). The  
193 fractions were then carefully concentrated under nitrogen flow to 0.5 ml with the  
194 concentration around 5-10 mg/ml for GC-MS analysis. The GC-MS system consists of

195 the Agilent 7890 GC and 5975C mass spectrometers. A DB-5MS column 50 m × 0.25  
196 mm × 0.25 µm was used. High purity helium (99.9995 %) was used as a carrier gas with  
197 a flow rate of 1.0 ml/min. The injector temperature was 300 °C. The injection volume  
198 was 1.0 µl. All injections were done with a 7683B series autosampler. The oven  
199 temperature was programmed from 50 °C (1 min hold) to 100°C at 10°C /min, and then  
200 to 310°C (20 min hold) at 2°C /min. The mass spectrometer was operated in the electron  
201 impact mode (70 eV). The temperature of ion source and transfer-line were set at 230°C  
202 and 300°C, respectively. The scanned mass range was from 50 to 550 u. The temperature  
203 of the quadrupole was held at 150°C.

204 For the oil Re-Os analysis, the asphaltene fraction was analyzed as Re and Os are  
205 predominantly contained within the asphaltene fraction of oil (Cumming et al., 2014;  
206 Georgiev et al., 2016; Lillis and Selby, 2013; Rooney et al., 2012; Selby et al., 2007). The  
207 asphaltene fraction was precipitated from the oil using 40 times volume of *n*-heptane  
208 (~1g oil with 40 ml solvent) at room temperature for at least 8 hrs. The Re and Os  
209 isotopic compositions and abundances of the asphaltene from the oil were analysed at the  
210 Laboratory for Source Rock and Sulfide Geochronology and Geochemistry and the  
211 Arthur Holmes Laboratory (members of the Durham Geochemistry Centre) at Durham  
212 University following published analytical procedures (Selby et al., 2005; Selby et al.,  
213 2007). Approximately 100-200 mg of asphaltene were dissolved and equilibrated with a  
214 known amount of a mixed <sup>185</sup>Re and <sup>190</sup>Os spike solution by inverse *aqua-regia* (3 ml  
215 HCl and 6 ml HNO<sub>3</sub>) in a Carius tube for 24 hours at 220°C. Osmium was isolated and  
216 purified from the inverse *aqua-regia* by CHCl<sub>3</sub> solvent extraction at room temperature  
217 and micro-distillation. The Re was isolated using HCl-HNO<sub>3</sub>-based anion

218 chromatography. The purified Re and Os were loaded on Ni and Pt filaments,  
219 respectively, and analyzed using negative ion thermal ionization mass spectrometry  
220 (NTIMS). Total procedural blanks for Re and Os are  $1.60 \pm 0.03$  pg and  $0.05 \pm 0.01$  pg,  
221 respectively, with an average  $^{187}\text{Os}/^{188}\text{Os}$  ratio of  $0.22 \pm 0.06$  (1 SD;  $n = 4$ ). All  
222 uncertainties include the propagated uncertainty in sample and tracer solution weights,  
223 the standard, spike calibrations, mass spectrometry measurements, and blanks. In-house  
224 Re (Restd) and Os (DROsS) solutions were analyzed as a monitor of reproducibility of  
225 isotope measurements. The  $^{187}\text{Os}/^{188}\text{Os}$  values of the Os standard solution DROsS during  
226 this study are  $0.1611 \pm 0.0004$  (1SD,  $n = 126$ ), with the  $^{185}\text{Re}/^{187}\text{Re}$  values of the Re  
227 standard solution being  $0.5989 \pm 0.0019$  (1SD,  $n = 116$ ). These values are in agreement  
228 with those previously published for DROsS and Restd (Cumming et al., 2014; Finlay et  
229 al., 2011, 2012; Lillis and Selby, 2013; Nowell et al., 2008). The Re–Os data of this study  
230 are regressed using the program *Isoplot* V. 4.15 (Ludwig, 2003) with  $^{187}\text{Re}$  decay constant  
231 of  $1.666 \times 10^{-11} \text{a}^{-1}$  (Smoliar et al., 1996). The input data contains  $^{187}\text{Re}/^{188}\text{Os}$  and  
232  $^{187}\text{Os}/^{188}\text{Os}$  ratios with their total absolute  $2\sigma$  level uncertainty and the associated error  
233 correlation, Rho (Ludwig, 1980).

234 A doubly polished fluid inclusion wafer (~100 micron thick) of a bioclastic limestone  
235 from the Ordovician Yijianfang Formation from well Ha9 was prepared for the fluid  
236 inclusion studies (Fig 3). Fluid inclusion petrography, microthermometry, laser raman  
237 microspectroscopy (LRM) and confocal scanning laser microscopy (CSLM) were  
238 conducted by CV Associés Engineering, Nancy, France.

239 Fluid inclusion petrography was carried out using a Zeiss Axiovert 200 microscope  
240 equipped with both transmitted white and incident ultraviolet light (UV) ( $\lambda = 365$  nm). A

241 calibrated Linkam MDS 600 heating and cooling stage was used for microthermometry.  
242 Homogenization temperatures ( $T_h$ ) were obtained using the thermal cycling method with  
243 a heating rate of 10 °C/min (Goldstein and Reynolds, 1994). The measured temperature  
244 precision for the  $T_h$  is  $\pm 0.1$  °C. The LRM analyses of aqueous fluid inclusions were  
245 performed on a Labram Jobin Yvon spectrometer, using 514.5 nm radiation produced by  
246 an argon laser. The salinity of aqueous fluid was estimated by LRM following the method  
247 described by (Dubessy et al., 2002). The CSLM methodology was used to measure the  
248 gas/oil volume ratio ( $F_v$ ) of the hydrocarbon inclusions previously identified by UV-  
249 fluorescence and characterized by microthermometry. The measurements were carried  
250 out using a Bio-Rad (Zeiss) Radiance 2100 Rainbow confocal scanning laser microscope  
251 equipped with an argon laser emitting at 488 nm and mounted on a Nikon TE2000-U  
252 inverted microscope.

253

## 254 **4 Results**

### 255 **4.1 GC-MS analysis**

256 Abundant biomarkers (e.g., alkane and isoprenoids, terpane and steroids) were detected  
257 in all five oil samples (Table 2). The saturate fraction gas chromatograms (SFGCs) for  
258 three of the oils (Ha9, Ha701, XK4-3) exhibit an unresolved complex mixture (UCM)  
259 (Fig. 4), however, abundant alkane compounds are still detected in the oil samples above  
260 the UCM (Fig. 4). The carbon number of the alkane distributed between  $nC_{12}$  and  $nC_{27}$ ,  
261 with the highest peak occurring at  $nC_{15}$  or  $nC_{16}$  (Fig. 4). For the isoprenoids, the Pristane  
262 (Pr)/Phytane(Ph) ratios of the five oil samples range between 0.68 and 0.97. The ratios of  
263 Pr/ $nC_{17}$  and Ph/ $nC_{18}$  range from 0.04 - 0.47 and 0.07- 0.64, respectively (Table 2)(Fig.

264 5A, B). Tricyclic terpanes, tetracyclic terpanes and hopanes were detected in the oil  
265 samples ( $m/z$  191) (Fig. 4). The tricyclic terpanes range from  $C_{19}$  to  $C_{30}$ , with a clear  
266 abundance increase between  $C_{20}$ ,  $C_{21}$ , and  $C_{23}$  compounds (Fig. 4). The  $C_{24}$  tetracyclic  
267 terpane ( $C_{24}$ TET) is detected in the oils. The ratios of  $C_{19}/C_{23}$  tricyclic terpane  
268 ( $C_{19}$ TT/ $C_{23}$ TT), and  $C_{24}$  tetracyclic /  $C_{26}$  tricyclics terpane ( $C_{24}$ TET/  $C_{26}$ TT) are  
269 respectively 0.12 to 0.20 and 0.42 to 0.49 (Table 2)(Fig. 5C). The hopanes range from  
270  $C_{27}$  to  $C_{35}$  and exhibit the highest peaks at either  $C_{29}$  or  $C_{30}$ . The hopanes show a decrease  
271 in the abundance with increasing carbon number between  $C_{31}$  and  $C_{35}$  (Fig. 4). Additional  
272 compounds (e.g.,  $C_{30}$  diahopane ( $C_{30}$ DH), Ts (18 $\alpha$ (H)-trisorhopane), Tm (17 $\alpha$ (H)-  
273 trisorhopane), gammacerane and 25-nor-hopane) are also detected. The Ts/(Ts+Tm) and  
274  $C_{30}$ DH/ $C_{30}$ H ( $C_{30}$  hopane) ratios vary from 0.37 to 0.55 (except for Ha15-2 which has a  
275 value of ~0.03) and 0.03 to 0.13, respectively (Table 2)(Fig. 5D). The  
276 gammacerane/ $C_{30}$ H ratio varies from 0.05 to 0.19, with an average of 0.12, and the 25-  
277 nor-hopane/ $C_{30}$ H ratios range from 0.15 to 2.61 (Table 2)(Fig. 5F). Sterane compounds,  
278 such as  $C_{21}$  pregnane ( $C_{21}$ P),  $C_{22}$  homopregnane ( $C_{22}$ HP), diasterane, and  $C_{27}$ - $C_{29}$  sterane  
279 are detected (Fig. 4). The ratio of pregnane/homopregnane ( $C_{21}$ P/ $C_{22}$ HP) ranges from  
280 2.98 to 5.69, with an average of 4.03. The  $C_{27}$ ,  $C_{28}$ ,  $C_{29}$  sterane content of all the oil  
281 samples present a similar V-shape distribution, which display ~50.2, 14.6 and 35.1 %,   
282 respectively, with  $C_{27}$  sterane exhibiting the greatest abundance. The ratio of  $C_{29}\alpha\alpha\alpha$   
283  $20S/(20S+20R)$  and  $C_{29}\beta\beta/(\beta\beta+\alpha\alpha)$  vary from 0.30 to 0.48 and 0.55 to 0.58 (Fig. 5E).

#### 284 4.2 Fluid inclusion analysis

285 The fluid inclusion wafer from well Ha9 is composed of grains (mainly ooids,  
286 echinoderms and mollusks) enclosed by micrite and coarse calcite cements. Fluid

287 inclusions in both the cement and calcite replaced grains were studied. The majority of  
288 the hydrocarbon and aqueous inclusions are distributed along annealed microfractures  
289 both in the calcite cements and the calcite replaced grains. Hydrocarbon-bearing  
290 inclusions (typically  $\leq 5\mu\text{m}$  wide and  $\sim 2$  to  $10\mu\text{m}$  long; Fig. 3) are liquid-rich, two-phase  
291 (L+V; L>V) inclusions that display blue, green and yellow UV fluorescence and are  
292 brown in transmitted light. Some localized inclusions within the same crystal possess  
293 highly variable liquid/vapor ratio indicating late alteration events (leakage and/or necking  
294 down) (Table 3).

295 The majority of the aqueous inclusions are two-phase liquid rich inclusions (L+V; L>V)  
296 (Fig. 3). Rare monophasic liquid-rich aqueous inclusions were also encountered. All the  
297 fluid inclusions are  $\leq 5\mu\text{m}$  wide and  $\sim 2$  to  $15\mu\text{m}$  long. Both aqueous and hydrocarbon  
298 inclusions commonly occur along the same annealed microfractures indicating a coeval  
299 relationship between the fluids.

300 The homogenization temperatures ( $T_h$ ) values of the hydrocarbon-bearing inclusions  
301 range from  $24.6$  to  $122\text{ }^\circ\text{C}$  (Table 3), with the majority homogenizing between  $24.6$  and  
302  $79.9\text{ }^\circ\text{C}$  (Fig. 6A). The aqueous inclusions homogenize between  $61.2$  and  $141.0\text{ }^\circ\text{C}$  (Fig.  
303 6A). The aqueous inclusions that are coeval with the hydrocarbon-bearing inclusions  
304 homogenize between  $61.2$  and  $102.3\text{ }^\circ\text{C}$ , with a mean  $T_h$  of  $82.1\text{ }^\circ\text{C}$  (Fig. 6A). The  
305 calculated salinities obtained using the method of Dubessy et al., 2002 vary from  $6.7$  to  
306  $20.4\text{ wt. \% NaCl eq.}$  (Table 3), with the majority yielding values between  $12$  and  $16$   
307  $\text{wt. \% NaCl eq.}$  The coeval hydrocarbon and aqueous inclusions have salinity values  
308 between  $8.6$  and  $15.1\text{ wt. \% NaCl eq}$  (Fig. 6B).

309 The gas/oil volume ratio ( $F_v$ ) measured by confocal scanning laser microscopy (CSLM)

310 of three hydrocarbon-bearing inclusions, (ranging in size between 22 and 302  $\mu\text{m}^3$ ),  
311 ranges from 5.1 to 10.9 %. The bubble and bulk volumes of the hydrocarbon inclusions  
312 range between 1.8 and 5.6  $\mu\text{m}^3$ , and 22.0 and 84.4  $\mu\text{m}^3$  (Table 3). In general, a positive  
313 relationship exists between the Th and Fv data (Fig. 6C).

314 LRM analysis was conducted on 14 aqueous inclusions. One coeval aqueous inclusion  
315 with a Th of 83.2 °C (similar to the mean data, 82.1 °C) was characterized and used for  
316 the estimation of trapping conditions of both aqueous and hydrocarbon fluids (Table 3,  
317 Fig. 7C). The CH<sub>4</sub> content and salinity measurement were performed on 11 aqueous  
318 inclusions in calcite. Only two samples possess CH<sub>4</sub> above the detection limit (0.017 and  
319 0.075 molal) (Table 3). Both aqueous inclusion thermodynamic (AIT) modeling using the  
320 CH<sub>4</sub>-H<sub>2</sub>O-NaCl system (Duan et al., 1992; Guillaume et al., 2003), and hydrocarbon  
321 bearing fluid inclusion thermodynamic (PIT) modeling were used to estimate aqueous  
322 and hydrocarbon fluid trapping conditions (Montel, 1993; Pironon, 2004) in well Ha9 in  
323 the Halahatang oilfield (Fig. 7C).

#### 324 4.3 Re-Os analysis

325 The asphaltene Re and Os abundances of the five oil samples vary between 0.06 and 9.47  
326 ppb, and 4.9 and 57.2 ppt, respectively (Table 4). Both the Re and Os abundances of  
327 some of the oil samples are lower than those previously reported for oil and bitumen  
328 from both hydrocarbon or metalliferous systems (Cumming et al., 2014; Finlay et al.,  
329 2011; Ge et al., 2016; Georgiev et al., 2016; Lillis and Selby, 2013; Selby et al., 2005),  
330 with most of the samples possessing higher Re and Os abundances when compared with  
331 that of the average upper crust (Re: 0.198 ppb and Os: 31 ppt) (Esser and Turekian, 1993;  
332 Rudnick and Gao, 2003).

333 The  $^{187}\text{Re}/^{188}\text{Os}$  values of the oil range from ~78 to 1655 and exhibit a radiogenic  
334  $^{187}\text{Os}/^{188}\text{Os}$  composition of 1.48 to 4.68 (Table 4). Repeat analysis of oil samples Ha9 and  
335 Ha15-2, using a separately isolated asphaltene fraction, yield very reproducible  
336  $^{187}\text{Re}/^{188}\text{Os}$  (125.4 vs 125.2 and 1655.2 vs 1636.7) and  $^{187}\text{Os}/^{188}\text{Os}$  (1.66 vs 1.74 and 2.25  
337 vs 2.25) values, and similar Re (0.81 vs 1.23 ppb and 9.47 vs 5.86 ppb) and Os (37.4 vs  
338 57.2 ppt and 35.2 vs 22.0 ppt) abundances (Table 4). Similar reproducibility has also  
339 been shown by previous studies (Lillis and Selby, 2013; Liu et al., 2018; Selby et al.,  
340 2005).

341 Collectively all the Re-Os data of all five oil samples do not yield any meaningful date  
342 (Fig. 8) as sample Ha15-2 possesses a distinct Re-Os isotope composition to the  
343 remaining four oil samples that display a positive correlation between  $^{187}\text{Re}/^{188}\text{Os}$  and  
344  $^{187}\text{Os}/^{188}\text{Os}$  (Fig. 8). The Re-Os data, without sample Ha15-2, yield a Model 3 (assumes  
345 that the scatter in the degree of fit of the data is a combination of the assigned  
346 uncertainties, plus a normally distributed variation in the  $^{187}\text{Os}/^{188}\text{Os}$  values (Ludwig,  
347 2008) date of  $285 \pm 48$  Ma ( $n = 5$ , MSWD = 6.1), with an initial  $^{187}\text{Os}/^{188}\text{Os}$  composition  
348 of  $1.08 \pm 0.20$  (Fig. 8).

349

## 350 **5 Discussion**

### 351 **5.1 Oil Geochemistry of the Halahatang Oilfield**

352 The biomarker molecular composition of an oil (*n*-alkanes, terpane, sterane) records  
353 information about its origin, maturity and alteration (Peters and Moldowan, 1993b; Wu et  
354 al., 2012; Zumberge, 1987). The carbon number of the alkane distributed between  $n\text{C}_{12}$   
355 and  $n\text{C}_{27}$ , with the highest peak occurring at  $n\text{C}_{15}$  or  $n\text{C}_{16}$  (Fig. 4), indicating the oil is

356 mainly sourced from bacteria and algae (Peters et al., 2005). The ratios of Pr/nC<sub>17</sub> and  
357 Ph/nC<sub>18</sub> range from 0.04 - 0.47 and 0.07- 0.64, respectively (Table 2) (Fig. 5A) and  
358 indicate the oils are from marine or saline facies sourced from lower bacteria and algae  
359 (Zhang et al., 2011). The pristane/phytane (Pr/Ph) ratio is a useful parameter to establish  
360 the depositional environment of the source unit of the oil. As such, Pr/Ph values of <1.0  
361 and >3.0 are suggested to indicate either an anoxic or oxic depositional environment,  
362 respectively (Didyk et al., 1978; Hunt, 1995; Peters et al., 2005). The Pr/Ph ratios of the  
363 Halahatang oils (0.68 - 0.97) (Fig. 5B) suggest that the oils are derived from a source unit  
364 deposited under predominantly anoxic conditions in a marine environment. The similar  
365 ratios of tricyclic terpanes (e.g., C<sub>23</sub>/C<sub>21</sub> tricyclic terpanes (C<sub>23</sub>TT/C<sub>21</sub>TT) (~2.05), C<sub>23</sub>/C<sub>24</sub>  
366 tricyclic terpanes (C<sub>23</sub>TT/C<sub>24</sub>TT)(~1.73), C<sub>19</sub>/C<sub>23</sub> tricyclic terpanes (C<sub>19</sub>TT/C<sub>23</sub>TT)  
367 (~0.16) and the C<sub>24</sub> tetracyclic / C<sub>26</sub> tricyclics terpane (C<sub>24</sub>TET/C<sub>26</sub>TT) (~0.45) (Table 2)  
368 (Fig.5C)) suggest that the oils belong to one family. The low ratios of C<sub>19</sub>/C<sub>23</sub> tricyclic  
369 terpane (C<sub>19</sub>TT/C<sub>23</sub>TT) (0.12 - 0.20), and C<sub>24</sub> tetracyclic / C<sub>26</sub> tricyclics terpane (C<sub>24</sub>TET/  
370 C<sub>26</sub>TT)(0.42 - 0.49) suggest that the oil samples are derived from a source containing  
371 marine derived organic matter (Bao et al., 2012; Peters and Moldowan, 1993a; Zumberge,  
372 1987) (Table 2)(Fig. 5C). In addition, the similar C<sub>21</sub>/C<sub>22</sub> sterane (C<sub>21</sub>P/C<sub>22</sub>HP) ratio  
373 (>3.0) of the oil samples is also indicative that the oils belong to the same family (Table  
374 2). The relative abundance of the C<sub>27</sub>, C<sub>28</sub>, C<sub>29</sub> regular steranes are used to constrain the  
375 source types, with the C<sub>27</sub> sterane being linked to a marine planktonic source and the C<sub>29</sub>  
376 sterane, although they can be derived from algae, is mainly sourced from higher  
377 terrestrial plants (Peters and Moldowan, 1993a). The V-shape distribution of the C<sub>27</sub>, C<sub>28</sub>,  
378 C<sub>29</sub> regular steranes, with C<sub>27</sub> possessing the largest component on the Halahatang oils

379 imply that the organic matter of the source has an alga source (Fig. 4) (Peters and  
380 Moldowan, 1993a). As Ts and diahopane are more resistant to thermal stress than Tm and  
381 hopane, the  $Ts / (Ts+Tm)$  and diahopane/ hopane ( $C_{30}DH/C_{30}H$ ) ratios can provide  
382 insights to the level of oil maturity, with lower ratios equating to lower levels of maturity  
383 (Lu et al., 2010; Peters and Moldowan, 1993a). The  $Ts / (Ts + Tm)$  (~0.34) and  
384  $C_{30}DH/C_{30}H$  (~0.09) ratios of the Halahatang oil samples indicate the oils are low to  
385 moderate maturity (Table 2). The  $C_{29}$  sterane is also a vital biomarker to determine the  
386 level of hydrocarbon maturity (Brooks and Welte, 1984; Peters and Moldowan, 1993a).  
387 The value of  $C_{29}\alpha\alpha/20S/(20S+20R)$  (~0.43) and  $C_{29}\beta\beta/(\beta\beta+\alpha\alpha)$  (~0.57) of the Halahatang  
388 oils (Fig. 5E) equates to a vitrinite reflectance ( $R_o$ ) values of ~0.8 and 0.9, and implies  
389 the oils are within the oil window maturity. The unresolved complex mixture (UCM) of  
390 the gas chromatograms shown by samples Ha9, Ha701 and XK4-3, as well as, the  
391 presence of  $C_{29}$  25-nor-hopane, with  $Nor25H/C_{30}H$  ratios of ~0.98, indicate the  
392 Halahatang oils have suffered biodegradation (Table 2) (Fig. 5F) (Wenger and Isaksen,  
393 2002). However, the relatively complete *n*-alkane compositions of the unresolved  
394 complex mixture indicate a second oil migration and accumulation event may have  
395 occurred in the Halahatang oilfield (Lu et al., 2008; Xiao et al., 2013; Zhu et al., 2012)  
396 (Fig. 4). In the case of the Ha15-2 oil, although the majority of biomarker parameters  
397 possess similar characteristics to the other four Halahatang oil samples, its distinct  
398 maturity ( $Ts / (Ts+Tm) = 0.03$ ) and biodegradation related parameters ( $C_{29}Nor_{25}H/C_{30}H =$   
399 ~0.15) (Table 2) indicate that sample Ha15-2 may have experienced alteration after the  
400 oil reservoir formed. However, as there is no obvious UCM found and that the sample  
401 possesses the lowest  $C_{29}Nor_{25}H/C_{30}H$  value (0.15) (Fig. 4), thermal degradation rather

402 than the biodegradation may be the main alteration mechanism. In summary, the GC-MS  
403 data show that the Halahatang oils belong to one family, derived from the same source  
404 that was deposited in a marine environment. In general, the oils are of low to moderate  
405 maturity, biodegraded, and may have experienced second hydrocarbon migration event.  
406 The organic geochemical differences of oil sample Ha15-2 indicate that some of the oil  
407 within the Halahatang oilfield may have undergone alteration after oil generation.

## 408 **5.2 Petroleum evolution timing constraints of the Halahatang Oilfield**

409 Fluid inclusions represent micron scale samples of the fluids (oil, gas and water) that  
410 migrated through and interacted with the host rocks during the evolution of a  
411 hydrocarbon system in sedimentary basins (Cooley et al., 2011). Fluid inclusion studies  
412 can play a key role in developing pressure, temperature, volume and composition models  
413 of fluid (oil and aqueous fluids) dynamics in petroliferous basins. Furthermore, fluid  
414 inclusion studies are critical to the understanding of petroleum migration and  
415 accumulation, and can help to predict the distribution of petroleum resources (Aplin et  
416 al., 1999; Bodnar, 1990; Bourdet et al., 2010; Oxtoby et al., 1995; Pironon, 2004;  
417 Teinturier et al., 2002). This study uses aqueous, and hydrocarbon bearing fluid  
418 inclusions to help elucidate the history of petroleum and aqueous fluid dynamics in the  
419 Tarim basin.

420 The majority of the hydrocarbon-bearing fluid inclusions of this study exhibit yellow  
421 fluorescence, however, some green, and blue fluorescing inclusions are also encountered  
422 (Fig. 3). This indicates that the majority oil in the fluid inclusions is of low maturity.  
423 Indeed, hydrocarbons of different maturity or having experienced multiple migration  
424 events commonly exhibit a range of fluorescence colors (Burruss, 1985; Chen, 2014;

425 McLimans, 1987; Stasiuk and Snowdon, 1997). Therefore, unlike the previous fluid  
426 inclusion results from the Yingmaili oilfield, west of the Halahatang oilfield (Zhu et al.,  
427 2013a), the fluid inclusions of this study indicate that the Halahatang oilfield experienced  
428 a complex history of hydrocarbon evolution. For example, the blue fluorescing high  
429 maturity oil in some of the hydrocarbon bearing inclusions, although uncommon, maybe  
430 related to late stage hydrocarbon migration (Guo et al., 2016; Shi et al., 2015; Su et al.,  
431 1991).

432 The Th-salinity bivariate plot (Fig. 6B) for the aqueous FIs defines two groups: a low Th  
433 (<100 °C) with <15 wt % NaCl eq. fluid and a fluid with Th >110 °C and a salinity range  
434 between ~6 and 22 wt % NaCl eq. This division may reflect at least two stages of  
435 aqueous fluid movement. The broad range in Th values of the hydrocarbon bearing  
436 inclusions (~24 - 122 °C) may reflect post-entrapment changes to the inclusion bearing  
437 fluid. This is further supported by the positive correlation between the vapor bubble  
438 volume percent (Fv % at 20 °C) and the Th values (Fig. 6C) (Bourdet et al., 2008). The  
439 measured inclusions with the highest Th (>100 °C) also have the highest Fv (13.9 %)  
440 values indicating post-entrapment modification. Furthermore, homogenization  
441 temperatures can decrease due to post-entrapment thermal cracking (Okubo, 2005). In  
442 our study, the two hydrocarbon bearing inclusions with the lowest Th values (~25 °C and  
443 43 °C) also possess the highest CH<sub>4</sub> volume (~95 and 84 μm<sup>3</sup>, Table 3), which may  
444 indicate that some of the oils in the Halahatang oilfield have experienced thermal  
445 cracking. In general, the Th of hydrocarbon bearing fluid inclusions can also be modified  
446 by other post-entrapment events or processes e.g.: necking-down and re-equilibration  
447 (Bourdet et al., 2008; Larson et al., 1973). Therefore, the Th of the aqueous fluid

448 inclusions that are coeval with the hydrocarbon-bearing inclusions are used to constrain  
449 the trapping temperature of the fluid that is saturated with CH<sub>4</sub> (Nedkvitne et al., 1993;  
450 Visser, 1982). The isochores and isopleths for the aqueous inclusions are plotted as the  
451 dash-point lines in P-T space (Fig. 7C). For comparison, isochores are also drawn for  
452 non-coeval aqueous inclusions in Figure 7C. The aqueous inclusions coeval with the  
453 hydrocarbon-bearing inclusions display a unimodal Th distribution (~61 to 102 °C; mean  
454 Th = 82.1 °C, n = 23) (Fig. 7B). Two Th values were used to model the fluid trapping  
455 conditions (Fig. 7C) i.e. Th of 83.2 °C (a coeval aqueous inclusion) the other represents  
456 the mean Th value (~82.0°C). The solid lines in Figure 6C are the isochores (and  
457 isopleths) for the three oil bearing inclusions plotted in Figure 5C. The intersections of  
458 the isochores for the oil-bearing inclusion (solid lines, Fig. 7C) and the selected coeval  
459 aqueous inclusions provide estimated fluid trapping temperatures of 100 to 110 °C and  
460 fluid trapping pressures of ~39 to 59 MPa (Fig. 7C).

461 Basin modelling coupled with fluid inclusion analysis has been widely applied to  
462 constrain the timing of hydrocarbon charging in petroleum systems (Cao et al., 2006;  
463 Guo et al., 2012; Roberts et al., 2004). In the Halahatang depression, basin modelling  
464 based on wells Ha601 and Ha9 suggest that the Early Palaeozoic source units were buried  
465 to ~3500 m (11,483 ft) and underwent hydrocarbon maturation between the  
466 Carboniferous and Permian (Zhang et al., 2007a; Zhu et al., 2012). Plotting the modelled  
467 Th data from this study with the previous basin model, one prolonged oil migration event  
468 during the Permian is proposed (Fig. 7A), which agrees with previous fluid inclusion  
469 studies of the Halahatang depression that also indicated the migration of hydrocarbons  
470 during the Late Permian (Xiao et al., 2012).

471 Authigenic illite is one of the last phases formed mineral cements prior to hydrocarbon  
472 migration into a sandstone reservoir (Hamilton et al., 1989). If the displacement of an  
473 aqueous pore fluid is replaced by hydrocarbons this leads to the cessation of illite  
474 formation (Lee et al., 1985). The last formed illite can be used to determine the maximum  
475 timing of hydrocarbon emplacement or migration (Hogg et al., 1993). Among the many  
476 diagenetic clay mineral products amenable for geochronology, illite is the only commonly  
477 occurring diagenetic mineral in sandstone reservoirs that contain sufficient long-lived  
478 radioisotope ( $^{40}\text{K}$ ), which permit the determination of its formation age (Hamilton et al.,  
479 1989). Although there is no sandstone reservoir in the Halahatang depression, in the  
480 Yingmaili Oilfield, ~30 km (~18.6 mi) northwest of the Halahatang depression, the  
481 Silurian Keping Formation sandstone reservoir is well-developed (Li et al., 2009). This  
482 sandstone strata is a reservoir to bitumen/oil and gas (Zhang and Luo, 2011).  
483 Hydrocarbons of the Silurian Keping Formation share a similar origin to hydrocarbons  
484 reservoired in Ordovician strata and thus may have charged at the same time (Zhu et al.,  
485 2013a). Published illite K-Ar isotope data in the Keping Formation sandstone reservoir  
486 (Zhang and Luo, 2011; Zhu et al., 2012) could aid in understanding the petroleum  
487 evolution (migration) in the Halahatang oilfield. Seven sandstone samples from different  
488 wells (YM11, YM34, YM35, YM35-1) and depths (Fig. 1C) show a decreasing age trend  
489 from the northwest ( $293 \pm 2$ ) to the southeast ( $255 \pm 3$  Ma) (Zhang and Luo, 2011; Zhu et  
490 al., 2012). The much younger illite K-Ar date than the deposition age of the Keping  
491 Formation indicates the sandstone samples contain no or little detrital illitic  
492 contamination and that the K-Ar date obtained from the fine fraction should  
493 approximately reflect the timing of diagenetic illite formation. Except for the Yingmaili

494 oilfield which is near to the Halahatang oilfield, other K-Ar dates in Tarim Basin, e.g., the  
495 Hadexun oilfield in the Northern Depression and Tazhong oilfield, respectively ~50 km  
496 (~31 mi) and ~100 km (~62 mi) south to the Hahalatang depression (Fig. 1B), also  
497 possess illite K-Ar dates of ~250 Ma and ~230 Ma, respectively (Zhang et al., 2007b;  
498 Zhu et al., 2013b). All the illite K-Ar dates (~280 - 230 Ma) from the central and northern  
499 Tarim Basin coincide with the above fluid inclusion and basin modelling data that show  
500 the major hydrocarbon migration and accumulation occurred predominantly during  
501 between the Mid to Late Permian.

502 Petroleum evolution is a complex process including oil generation, migration and finally  
503 accumulation or destruction. Oil generation, which leads the whole evolution process, is  
504 one key factor. Previous research has shown that oil generation is a multi-step procedure  
505 involving bitumen formation from the kerogen and oil generation from the bitumen, and  
506 that these two steps are closely related (Lewan, 1985). Oil/bitumen/pyrobitumen Re-Os  
507 analysis, which is a new and challenging method, has shown potential in constraining the  
508 absolute timing of the oil/bitumen/pyrobitumen generation (Cumming et al., 2014; Finlay  
509 et al., 2011; Ge et al., 2016; Lillis and Selby, 2013; Liu et al., 2018; Selby and Creaser,  
510 2005). Although the GC-MS analysis and fluid inclusion analysis indicate that some oil  
511 samples in this study have suffered from biodegradation and secondary migration,  
512 however, previous research has shown that biodegradation do not significantly affect the  
513 Re-Os systematics of oil (Lillis and Selby, 2013). Moreover, and if the oils generated  
514 during one period, then multiple oil migration episodes following the generation will not  
515 disturb the hydrocarbon Re-Os system (Finlay et al., 2011; Lillis and Selby, 2013; Selby  
516 et al., 2005).

517 The Re-Os data for all oil samples, except sample Ha15-2, yield a Model 3 Re-Os age of  
518  $285 \pm 48$  Ma ( $O_s_i = 1.08 \pm 0.20$  [18.5 %], MSWD = 6.1). The large age uncertainty  
519 (~17 %) and MSWD value is beyond that associated with analytical uncertainty (~1.0),  
520 and is considered to be directly related to the variation in the initial  $^{187}\text{Os}/^{188}\text{Os}$  ratio ( $O_s_i$ )  
521 of the sample set (Cohen et al., 1999; Ludwig, 2008) (Fig. 8; Table 4). Given that oils are  
522 generated from a source horizon that can be both stratigraphically (10s to 100s of m/ft)  
523 and geographically (10s to 100s kilometers/miles) expansive, the ability for oil sampled  
524 across a reservoir to possess the same initial  $O_s_i$  ratio can be challenged (see (Lillis and  
525 Selby, 2013)), but can also exhibit a limited range in values ((Liu et al., 2018 and  
526 references therein). The variation in  $O_s_i$  values could also relate to the oil sampled being  
527 associated with difference stages of the oil generation of a petroleum system (Liu et al.,  
528 2018).

529 The ~285 Ma Re-Os date, including its uncertainty of 48 Ma, is in good agreement with  
530 the understanding of the timing of oil generation in northern Tarim Basin (Zhu et al.,  
531 2013a; Zhu et al., 2012). Basin modelling both in the Halahatang and Yingmaili oilfields  
532 of the northern Tarim Basin, suggest that a Paleozoic source was buried to ~3000 m  
533 (~9842 ft) and underwent hydrocarbon maturation during the Late Carboniferous to Early  
534 Permian (Zhu et al., 2013a; Zhu et al., 2012). Although possessing a relatively large  
535 uncertainty (48 Ma), the ~285 Ma Re-Os date, which is nominally slightly older than the  
536 oil migration / accumulation timing constrained by basin modelling coupled with fluid  
537 inclusion analysis and the reservoir illite K-Ar dates (see above), suggests that the Re-Os  
538 date represents the best absolute estimate for the timing of oil generation in the  
539 Halahatang oilfield.

540 The oil sample Ha15-2 plots to right of the defined best-fit line (isochron) of the bulk of  
541 the Re-Os data for the oil sample set (Fig. 8). In comparison to the other oil samples,  
542 sample Ha15-2 also possesses different parameters in biomarker analysis  
543 ( $C_{29}NOR_{25}H/C_{30}H = 0.15$ ,  $Ts/(Ts+Tm) = 0.03$ ) indicating the sample has experience post-  
544 generation alteration. Furthermore, although of limited abundance, the presence of oil-  
545 bearing fluid inclusions with high Th ( $>120\text{ }^{\circ}C$ ) and a  $CH_4$  volume of  $\sim 90\text{ }\mu m^3$  of this  
546 study (Table 3) also indicate thermal cracking may have occurred in regions in the  
547 Halahatang oilfield. Moreover, the basin modelling shows that the Paleozoic strata in this  
548 area have been buried to  $\sim 7000\text{ m}$  ( $\sim 22,966\text{ ft}$ ) since the Late Neogene (Fig. 7A) (Zhu et  
549 al., 2012), and that during the last  $\sim 10$  Myrs the high temperatures ( $>150^{\circ}C$ ) may have  
550 led to thermal cracking of oil, particular in deeper parts, of the Halahatang oilfield (eg,  
551 Ha 15-2 oil). Previous work on TSR affected oil from the Manderson, South of the  
552 Bighorn Basin (Lillis and Selby, 2013) and pyrobitumen from Majiang - Wanshan  
553 reservoir, South China (Ge et al., 2016) have shown that the high temperature controlled  
554 thermal cracking can reset the Re-Os systematics in the hydrocarbons (oil/bitumen). The  
555 high Th and  $CH_4$  volume evidence from fluid inclusions, and basin modelling suggest  
556 that the thermal cracking which could lead to gas formation (Hill et al., 2003; Huc et al.,  
557 2000) may have resulted in the Re-Os characteristics shown by oil sample Ha15-2.  
558 Additional research on similar oils to Ha15-2 from the Halahatang oilfield will be  
559 necessary to see if the Re-Os systematics are still being effected by thermal cracking as it  
560 has been suggested the closure temperature of Re-Os in thermal cracked oil is  $\leq 120^{\circ}C$   
561 (Ge et al., 2016; Lillis and Selby, 2013).

### 562 **5.3 Petroleum evolution in the Halahatang depression**

563 Based on the general tectonic evolution of the Tarim Basin, and combining the oil Re-Os  
564 dating and fluid inclusion analysis of this study from the Halahatang depression, and  
565 previous basin modeling and illite K-Ar isotope dates from Tarim Basin, the petroleum  
566 evolution in the Halahatang depression can be summarized as follows. Exhumation of  
567 Silurian strata driven by the Caledonian Orogeny during the Devonian (Fig. 9A) (Lin et  
568 al., 2015), the Tarim Basin transferred into an extensional environment between the  
569 Carboniferous and Permian (Zhang et al., 2007a). The continued subsidence during this  
570 period led to the burial (>3500 m) (>11483 ft) of the Paleozoic source units (Cambrian to  
571 Ordovician shales/mudstone) and oil generation during the Early Permian (Fig. 9B)  
572 (~285 Ma Re-Os oil date). The closure of the Tian Shan Sea (Late Hercynian tectonic  
573 event) caused a phase of uplift and exhumation during the Mid-Late Permian that resulted  
574 in the cessation the oil generation (Lin et al., 2015; Zhang et al., 2007a). However,  
575 tectonic instability, as well as, the simultaneous formed faults provided pathways for oil  
576 migration and accumulation (Zhu et al., 2013c). Both basin modelling and coupled fluid  
577 inclusion analysis of this study and previous illite K-Ar dating (~280 - 230 Ma) within  
578 central and northern Tarim Basin (Zhang et al., 2007b; Zhang and Luo, 2011; Zhu et al.,  
579 2012; Zhu et al., 2013b) show that hydrocarbon migration and accumulation occurred  
580 predominantly during the Mid-Permian, but also during the Early Triassic (Fig. 9C). The  
581 Tarim Basin changed to a continental sedimentary depositional environment as of the  
582 Mesozoic (Zhang and Huang, 2005). The basin burial history of the Halahatang  
583 depression shows a continuous sedimentary deposition since the Late Triassic including a  
584 rapid sedimentation since the Neogene (Fig. 9D). This has resulted in the deep burial  
585 (~7000 m) (22965 ft) of the Ordovician reservoirs. The deep burial and high temperatures

586 (>150 °C) are suitable for oil cracking to occur. Both the high Th and CH<sub>4</sub> volume  
587 observed in oil-bearing fluid inclusion and the oil Re-Os isotope characteristics of Ha 15-  
588 2 oil show evidence of thermal cracking in parts of the Halahatang oilfield. However, the  
589 organic geochemistry (Fig. 4) (Table 2), fluid inclusion analysis (Fig. 3) (Table 3) and  
590 Re-Os data (Fig. 8) of this study suggests that thermal cracking of oil in the Halahatang  
591 depression is neither prolonged nor widespread.

592

## 593 **6 Conclusions**

594 Combining the organic geochemical analysis, fluid inclusion analysis and Re-Os isotope  
595 analysis of the Halahatang oilfield, in addition to previously published basin modeling  
596 and illite K-Ar dating in Tarim Basin, the petroleum evolution of the Halahatang oilfield,  
597 Northern Tarim Basin is quantitatively constrained. The organic geochemistry analyses  
598 show the oil samples belong to same family, with the oils derived from a source  
599 deposited in an anoxic marine environment, possess low to middle maturity and have  
600 undergone limited biodegradation. The ~285 Ma Re-Os date coincides with the  
601 hydrocarbon trap evolution, the Cambrian-Ordovician source rock maturation history  
602 (Zhang et al., 2007a), basin modelling result for the Halahatang depression, and the  
603 nearby Yingmai Basin indicating that the Re-Os data records the timing of oil generation.  
604 Traditional basin modelling coupled with fluid inclusion analysis are in good agreement  
605 with published illite K-Ar dates (280 - 230 Ma) (Zhang et al., 2007b; Zhang and Luo,  
606 2011; Zhu et al., 2012; Zhu et al., 2013b) in the Tarim basin and suggest that oil  
607 migration/accumulation occurred during the Mid-Permian to Early Triassic. The Re-Os  
608 geochemistry of Ha15-2, and oil-bearing fluid inclusion analysis suggest that some oils in

609 the Halahatang depression have experienced thermal cracking since the Neogene.  
610 Integrating fluid inclusion analysis, reservoir illite K-Ar dating and Re-Os oil analysis,  
611 this work quantitatively establishes the entire petroleum evolution (generation,  
612 migration/accumulation) process in the Halahatang depression of the northern Tarim  
613 Basin. In addition to Tarim basin, the coupled analysis of Re-Os oil geochronology with  
614 K-Ar dating and fluid inclusions is also applicable to petroleum systems worldwide to aid  
615 in the understanding of both the temporal and spatial evolution of hydrocarbon systems.

## 616 **References**

- 617 Aplin, A., G. Macleod, S. Larter, K. Pedersen, H. Sorensen, and T. Booth, 1999, Combined use of  
618 Confocal Laser Scanning Microscopy and PVT simulation for estimating the composition  
619 and physical properties of petroleum in fluid inclusions: *Marine and Petroleum Geology*, v. 16,  
620 p. 97-110, Doi. 10.1016/S0264-8172(98)00079-8.
- 621 Bao, J., J. Kong, C. Zhu, Q. Zhang, M. Li, Y. Lu, and W. Zhang, 2012, Geochemical Characteristics of a  
622 Novel Kind of Marine Oils from Tarim Basin: *Acta Sedimentologica Sinica*, v. 30, p. 580-587,  
623 Doi. 10.14027/j.cnki.cjxb.2012.03.009.
- 624 Bodnar, R. J., 1990, Petroleum Migration in the Miocene Monterey Formation, California, USA:  
625 Constraints from Fluid-Inclusion Studies: *Mineralogical Magazine*, v. 54, p. 295-304, Doi.  
626 10.1180/minmag.1990.054.375.15.
- 627 Bourdet, J., J. Pironon, G. Levresse, and J. Tritlla, 2008, Petroleum type determination through  
628 homogenization temperature and vapour volume fraction measurements in fluid inclusions:  
629 *Geofluids*, v. 8, p. 46-59, Doi. 10.1111/j.1468-8123.2007.00204.x.
- 630 Bourdet, J., J. Pironon, G. Levresse, and J. Tritlla, 2010, Petroleum accumulation and leakage in a  
631 deeply buried carbonate reservoir, Níspero field (Mexico): *Marine and Petroleum Geology*, v.  
632 27, p. 126-142, Doi. 10.1016/j.marpetgeo.2009.07.003.
- 633 Brooks, J., and D. Welte, 1984, *Advances in petroleum geochemistry*, Academic Press, 344 p.
- 634 Burruss, R. C., 1985, Timing of hydrocarbon migration: evidenced from fluid inclusions in calcite  
635 cements, tectonics and burial history: Harris, P.M. (Ed.), *Carbonates Cements*. Society of  
636 Economic Paleontologists and Mineralogists Special Publication, v. 26, p. 277-289, Doi.  
637 10.2110/pec.85.36.0277.
- 638 Cao, J., S. Yao, Z. Jin, W. Hu, Y. Zhang, X. Wang, Y. Zhang, and Y. Tang, 2006, Petroleum migration and  
639 mixing in the northwestern Junggar Basin (NW China): constraints from oil-bearing fluid  
640 inclusion analyses: *Organic Geochemistry*, v. 37, p. 827-846, Doi.  
641 10.1016/j.orggeochem.2006.02.003.
- 642 Chang, X., T.-G. Wang, Q. Li, B. Cheng, and X. Tao, 2013a, Geochemistry and possible origin of  
643 petroleum in Palaeozoic reservoirs from Halahatang Depression: *Journal of Asian Earth  
644 Sciences*, v. 74, p. 129-141, Doi. 10.1016/j.jseas.2013.03.024.
- 645 Chang, X., T. G. Wang, L. Qiming, and O. Guangxi, 2013b, Charging of Ordovician reservoirs in the  
646 Halahatang depression (Tarim Basin, NW China) determined by oil geochemistry: *Journal of  
647 Petroleum Geology*, v. 36, p. 383-398, Doi. 10.1111/jpg.12562.
- 648 Chen, H., 2014, Microspectrofluorimetric characterization and thermal maturity assessment of  
649 individual oil inclusion: *Acta Petrolei Sinica*, v. 35, p. 584-590, Doi. 10.7623/syxb201403023.
- 650 Cohen, A. S., A. L. Coe, J. M. Bartlett, and C. J. Hawkesworth, 1999, Precise Re-Os ages of organic-rich  
651 mudrocks and the Os isotope composition of Jurassic seawater: *Earth and Planetary Science  
652 Letters*, v. 167, p. 159-173, Doi. 10.1016/S0012-821X(99)00026-6.

653 Cooley, M. A., R. A. Price, T. K. Kyser, and J. M. Dixon, 2011, Stable-isotope geochemistry of syntectonic  
654 veins in Paleozoic carbonate rocks in the Livingstone Range anticlinorium and their  
655 significance to the thermal and fluid evolution of the southern Canadian foreland thrust and  
656 fold belt: AAPG Bulletin, v. 95, p. 1851-1882, Doi. 10.1306/01271107098.

657 Cui, H., D. Zheng, and T. Teng, 2009, Petroleum geologic characteristics and exploration orientation in  
658 Halahatang Depression of Tabei uplift: Lithologic Reservoirs v. 21, p. 54-58.

659 Cumming, V. M., D. Selby, P. G. Lillis, and M. D. Lewan, 2014, Re-Os geochronology and Os isotope  
660 fingerprinting of petroleum sourced from a Type I lacustrine kerogen: Insights from the  
661 natural Green River petroleum system in the Uinta Basin and hydrous pyrolysis experiments:  
662 *Geochimica et Cosmochimica Acta*, v. 138, p. 32-56, Doi. 10.1016/j.gca.2014.04.016.

663 Didyk, B. M., B. R. T. Simoneit, S. C. Brassell, and G. Eglinton, 1978, Organic geochemical indicators of  
664 palaeoenvironmental conditions of sedimentation: *Nature*, v. 272, p. 216-222, Doi.  
665 10.1038/272216a0.

666 Duan, Z., N. Møller, J. Greenberg, and J. H. Weare, 1992, The prediction of methane solubility in natural  
667 waters to high ionic strength from 0 to 250°C and from 0 to 1600 bar: *Geochimica et*  
668 *Cosmochimica Acta*, v. 56, p. 1451-1460, Doi. 10.1016/0016-7037(92)90215-5.

669 Duan, Z., and S. Mao, 2006, A thermodynamic model for calculating methane solubility, density and  
670 gas phase composition of methane-bearing aqueous fluids from 273 to 523 K and from 1 to  
671 2000 bar: *Geochimica et Cosmochimica Acta*, v. 70, p. 3369-3386, Doi.  
672 10.1016/j.gca.2006.03.018.

673 Dubessy, J., T. Lhomme, M.-C. Boiron, and F. Rull, 2002, Determination of Chlorinity in Aqueous Fluids  
674 Using Raman Spectroscopy of the Stretching Band of Water at Room Temperature:  
675 Application to Fluid Inclusions: *Applied Spectroscopy*, v. 56, p. 99-106, Doi.  
676 10.1366/0003702021954278.

677 Esser, B. K., and K. K. Turekian, 1993, The osmium isotopic composition of the continental crust:  
678 *Geochimica et Cosmochimica Acta*, v. 57, p. 3093-3104, Doi. 10.1016/0016-7037(93)90296-  
679 9.

680 Finlay, A. J., D. Selby, and M. J. Osborne, 2011, Re-Os geochronology and fingerprinting of United  
681 Kingdom Atlantic margin oil: Temporal implications for regional petroleum systems: *Geology*,  
682 v. 39, p. 475-478, Doi. 10.1130/G31781.1.

683 Finlay, A. J., D. Selby, and M. J. Osborne, 2012, Petroleum source rock identification of United Kingdom  
684 Atlantic Margin oil fields and the Western Canadian Oil Sands using Platinum, Palladium,  
685 Osmium and Rhenium: Implications for global petroleum systems: *Earth and Planetary*  
686 *Science Letters*, v. 313, p. 95-104, Doi. 10.1016/j.epsl.2011.11.003.

687 Ge, X., C. Shen, D. Selby, D. Deng, and L. Mei, 2016, Apatite fission-track and Re-Os geochronology of  
688 the Xuefeng uplift, China: Temporal implications for dry gas associated hydrocarbon systems:  
689 *Geology*, v. 44, p. 491-494, Doi. 10.1130/g37666.1.

690 Ge, X., C. Shen, D. Selby, G. Wang, Z. Yang, Y. Gong, and S. Xiong, 2018a, Neoproterozoic-Cambrian  
691 petroleum system evolution of the Micang Shan Uplift, Northern Sichuan Basin, China :  
692 insights from pyrobitumen Re-Os geochronology and apatite fission track analysis: AAPG  
693 Bulletin, v. 102, p. 1429-1453, Doi. 10.1306/1107171616617170.

694 Ge, X., C. Shen, D. Selby, J. Wang, L. Ma, X. Ruan, S. Hu, and L. Mei, 2018b, Petroleum generation timing  
695 and source in the Northern Longmen Shan Thrust Belt, Southwest China: Implications for  
696 multiple oil generation episodes and sources: AAPG Bulletin, v. 102, p. 913-938, Doi.  
697 10.1306/0711171623017125.

698 General Administration of Quality Supervision Inspection and Quarantine of the People's Republic of  
699 China, 2011, Density or relative density analysis methods on crude petroleum and liquid or  
700 solid petroleum products p. 17.

701 Georgiev, S. V., H. J. Stein, J. L. Hannah, R. Galimberti, M. Nali, G. Yang, and A. Zimmerman, 2016, Re-Os  
702 dating of maltenes and asphaltenes within single samples of crude oil: *Geochimica et*  
703 *Cosmochimica Acta*, v. 179, p. 53-75, Doi. 10.1016/j.gca.2016.01.016.

704 Goldstein, R., and T. Reynolds, 1994, Systematics of fluid inclusions in diagenetic minerals: SEPM  
705 (Society for Sedimentary Geology) Short Course 31, SEPM (Society for Sedimentary Geology).

706 Guillaume, D., S. Teinturier, J. Dubessy, and J. Pironon, 2003, Calibration of methane analysis by Raman  
707 spectroscopy in H<sub>2</sub>O-NaCl-CH<sub>4</sub> fluid inclusions: *Chemical Geology*, v. 194, p. 41-49, Doi.

708 10.1016/S0009-2541(02)00270-X.  
709 Guo, X., K. Liu, S. He, G. Song, Y. Wang, X. Hao, and B. Wang, 2012, Petroleum generation and charge  
710 history of the northern Dongying Depression, Bohai Bay Basin, China: Insight from integrated  
711 fluid inclusion analysis and basin modelling: *Marine and Petroleum Geology*, v. 32, p. 21-35,  
712 Doi. 10.1016/j.marpetgeo.2011.12.007.  
713 Guo, X., K. Liu, C. Jia, Y. Song, M. Zhao, Q. Zhuo, and X. Lu, 2016, Fluid evolution in the Dabei Gas Field  
714 of the Kuqa Depression, Tarim Basin, NW China: Implications for fault-related fluid flow:  
715 *Marine and Petroleum Geology*, v. 78, p. 1-16, Doi. 10.1016/j.marpetgeo.2016.08.024.  
716 Hamilton, P., S. Kelley, and A. E. Fallick, 1989, K-Ar dating of illite in hydrocarbon reservoirs: *Clay*  
717 *Minerals*, v. 24, p. 215-231, Doi. 10.1180/claymin.1989.024.2.08.  
718 Hill, R. J., Y. Tang, and I. R. Kaplan, 2003, Insights into oil cracking based on laboratory experiments:  
719 *Organic Geochemistry*, v. 34, p. 1651-1672, Doi. 10.1016/s0146-6380(03)00173-6.  
720 Hogg, A., P. Hamilton, and R. Macintyre, 1993, Mapping diagenetic fluid flow within a reservoir: K-Ar  
721 dating in the Alwyn area (UK North Sea): *Marine and Petroleum Geology*, v. 10, p. 279-294,  
722 Doi. 10.1016/0264-8172(93)90110-E.  
723 Huc, A. Y., P. Nederlof, R. Debarre, B. Carpentier, M. Boussafir, F. Laggoun-Défarge, A. Lenail-Chouteau,  
724 and N. Bordas-Le Floch, 2000, Pyrobitumen occurrence and formation in a Cambro-  
725 Ordovician sandstone reservoir, Fahud Salt Basin, North Oman: *Chemical Geology*, v. 168, p.  
726 99-112, Doi. 10.1016/S0009-2541(00)00190-X.  
727 Hunt, M., 1995, *Petroleum geochemistry and geology*, 2nd Edition: New York, NY, WH Freeman and  
728 company, 743 p.  
729 Huo, Z., T. Jiang, X. Pang, W. Wang, J. Chen, J. Song, W. Shen, and Z. Pan, 2016, Evaluation of Deep  
730 Carbonate Source Rocks with Low TOC and Contribution to Oil-Gas Accumulation in Tazhong  
731 Area, Tarim Basin: *Earth Science*, v. 41, p. 2061-2074, Doi. 10.3799/dqkx.2016.143.  
732 Jia, C., and G. Wei, 2002, Structural characteristics and petroliferous features of Tarim Basin: *Chinese*  
733 *Science Bulletin*, v. 47, p. 1-11, Doi. 10.1007/BF02902812.  
734 Larson, L. T., J. D. Miller, J. E. Nadeau, and E. Roedder, 1973, Two sources of error in low temperature  
735 inclusion homogenization determination, and corrections on published temperatures for the  
736 East Tennessee and Laisvall deposits: *Economic Geology*, v. 68, p. 113-116, Doi.  
737 10.2113/gsecongeo.68.1.113.  
738 Lee, M., J. L. Aronson, and S. M. Savin, 1985, K/Ar dating of time of gas emplacement in Rotliegendes  
739 sandstone, Netherlands: *AAPG Bulletin*, v. 69, p. 1381-1385.  
740 Lewan, M., 1985, Evaluation of petroleum generation by hydrous pyrolysis experimentation:  
741 *Philosophical Transactions of the Royal Society of London. Series A, Mathematical and*  
742 *Physical Sciences*, v. 315, p. 123-134, Doi. 10.1306/94886d71-1704-11d7-  
743 8645000102c1865d.  
744 Li, K., 2009, *The Three Main Paleohigh's Evolution and affection Hydrocarbon Accumulation, Tarim*  
745 *Basin*, Chengdu University of Technology, 157 p.  
746 Li, S., X. Pang, Z. Jin, H. Yang, Z. Xiao, Q. Gu, and B. Zhang, 2010, Petroleum source in the Tazhong  
747 Uplift, Tarim Basin: new insights from geochemical and fluid inclusion data: *Organic*  
748 *Geochemistry*, v. 41, p. 531-553, Doi. 10.1016/j.orggeochem.2010.02.018.  
749 Li, Y., C. Xie, X. Deng, and H. Guo, 2009, Reservoir characteristic and controlling factors of Silurian  
750 Kepingtage Formation in YM34 and YM35 well block: *Geology in China*, v. 26, p. 1087-1098.  
751 Liao, Z., L. Zhang, C. Yang, H. Zhang, T. Wang, and Y. Lu, 2010, Geochemical characteristics of heavy oils  
752 from the east and west sides of Halahatang Depression, Tarim Basin, China: Exemplified by  
753 oils of LG7 and DH1-6-9: *GEOCHIMICA*, v. 39, p. 149-153.  
754 Lillis, P. G., and D. Selby, 2013, Evaluation of the rhenium-osmium geochronometer in the Phosphoria  
755 petroleum system, Bighorn Basin of Wyoming and Montana, USA: *Geochimica et*  
756 *Cosmochimica Acta*, v. 118, p. 312-330, Doi. 10.1016/j.gca.2013.04.01  
757 Lin, B., X. Zhang, X. Xu, J. Yuan, Y. Neng, and J. Zhu, 2015, Features and effects of basement faults on  
758 deposition in the Tarim Basin: *Earth-Science Reviews*, v. 145, p. 43-55, Doi.  
759 10.1016/j.earscirev.2015.02.008.  
760 Liu, J., D. Selby, M. Obermajer, and A. Mort, 2018, Re-Os geochronology and oil-source correlation of  
761 Duvernay Petroleum System, Western Canada Sedimentary Basin: Implications for the  
762 application of the Re-Os geochronometer to petroleum systems: *AAPG Bulletin*, v. 108, p.

763 1627-1657, Doi. 10.1306/12081717105.  
764 Liu, W., J. Wang, C. Tao, G. Hu, L. Lu, and P. Wang, 2013, The Geochronology of Petroleum  
765 Accumulation of China Marine Sequence: *Natural Gas Geoscience*, v. 24, p. 199-209.  
766 Lu, J., S. Chen, X. Wang, L. Lu, X. Chen, and Y. Wang, 2010, Maturity study of the strong biodegradation  
767 viscous oil: taking the Santai-Beisantai area of Junggar Basin as an example. : *Petroleum  
768 Geology & Experiment*, v. 32, p. 373-376.  
769 Lu, Y., Z. Xiao, Q. Gu, and Q. Zhang, 2008, Geochemical characteristics and accumulation of marine oil  
770 and gas around Halahatang depression, Tarim Basin, China: *Science in China Series D: Earth  
771 Sciences*, v. 51, p. 195-206, Doi. 10.1007/s11430-008-5006-0.  
772 Ludwig, K., 2003, A plotting and regression program for radiogenic-isotope data, version 3.00: United  
773 State Geol Survey, open file report, p. 1-70.  
774 Ludwig, K., 2008, User's Manual for Isoplot 3.7: A geochronological toolkit for Microsoft Excel., v.  
775 Special Publication No.4: Berkeley Geochronological Centre, 76 p.  
776 Ludwig, K. R., 1980, Calculation of uncertainties of U-Pb isotope data: *Earth and Planetary Science  
777 Letters*, v. 46, p. 212-220, Doi. 10.1016/0012-821X(80)90007-2.  
778 Mark, D. F., J. Parnell, S. P. Kelley, M. R. Lee, and S. C. Sherlock, 2010, 40Ar/39Ar dating of oil  
779 generation and migration at complex continental margins: *Geology*, v. 38, p. 75-78, Doi.  
780 10.1130/G30237.1.  
781 McLimans, R. K., 1987, The application of fluid inclusions to migration of oil and diagenesis in  
782 petroleum reservoirs: *Applied Geochemistry*, v. 2, p. 585-603, Doi. 10.1016/0883-  
783 2927(87)90011-4.  
784 Montel, F., 1993, Phase equilibria needs for petroleum exploration and production industry: *Fluid  
785 Phase Equilibria*, v. 84, p. 343-367, Doi. 10.1016/0378-3812(93)85132-6.  
786 National Development and Reform Commission, 2008, Analysis method for fraction of rock extract  
787 and crude oil p. 8.  
788 National Energy Administration of the People's Republic of China, 1993, Analysis method for crude oil  
789 viscosity, p. 4.  
790 Nedkvitne, T., D. A. Karlsen, K. Bjørlykke, and S. R. Larter, 1993, Relationship between reservoir  
791 diagenetic evolution and petroleum emplacement in the Ula Field, North Sea: *Marine and  
792 Petroleum Geology*, v. 10, p. 255-270, Doi. 10.1016/0264-8172(93)90108-5.  
793 Nowell, G., D. Pearson, S. Parman, A. Lugué, and E. Hanski, 2008, Precise and accurate 186Os/188Os  
794 and 187Os/188Os measurements by multi-collector plasma ionisation mass spectrometry,  
795 part II: Laser ablation and its application to single-grain Pt-Os and Re-Os geochronology:  
796 *Chemical Geology*, v. 248, p. 394-426, Doi. 10.1016/j.chemgeo.2007.12.004.  
797 Okubo, S., 2005, Effects of thermal cracking of hydrocarbons on the homogenization temperature of  
798 fluid inclusions from the Niigata oil and gas fields, Japan: *Applied Geochemistry*, v. 20, p. 255-  
799 260, Doi. 10.1016/j.apgeochem.2004.09.001.  
800 Oxtoby, N. H., A. W. Mitchell, and J. G. Gluyas, 1995, The filling and emptying of the Ula Oilfield: fluid  
801 inclusion constraints: *Geological Society Special Publications*, v. 86, p. 141-157, Doi.  
802 10.1144/GSL.SP.1995.086.01.11.  
803 Peters, K., C. Walters, and J. Moldowan, 2005, *The Biomarker guide, biomarkers and isotopes in  
804 petroleum exploration and earth history, vol 1-2*, Cambridge University Press, New York, 961  
805 p.  
806 Peters, K. E., and J. M. Moldowan, 1993a, *The biomarker guide: interpreting molecular fossils in  
807 petroleum and ancient sediments*, Englewood Cliffs, NJ (United States); Prentice Hall.  
808 Peters, K. E., and J. M. Moldowan, 1993b, *The biomarker guide: interpreting molecular fossils in  
809 petroleum and ancient sediments: United States*, Englewood Cliffs, NJ (United States);  
810 Prentice Hall, 363 p.  
811 Pironon, J., 2004, Fluid inclusions in petroleum environments: analytical procedure for PTX  
812 reconstruction: *Acta Petrolei Sinica*, v. 20, p. 1332-1342.  
813 Qiu, H.-N., H.-Y. Wu, J.-B. Yun, Z.-H. Feng, Y.-G. Xu, L.-F. Mei, and J. Wijbrans, 2011, High-precision  
814 40Ar/39Ar age of the gas emplacement into the Songliao Basin: *Geology*, v. 39, p. 451-454,  
815 Doi. 10.1130/G31885.1.  
816 Roberts, L. N., M. D. Lewan, and T. M. Finn, 2004, Timing of oil and gas generation of petroleum  
817 systems in the Southwestern Wyoming Province: *Mountain Geologist*, p. 87-117.

818 Rooney, A. D., D. Selby, M. D. Lewan, P. G. Lillis, and J.-P. Houzay, 2012, Evaluating Re–Os systematics in  
819 organic-rich sedimentary rocks in response to petroleum generation using hydrous pyrolysis  
820 experiments: *Geochimica et Cosmochimica Acta*, v. 77, p. 275-291, Doi.  
821 10.1016/j.gca.2011.11.006.

822 Rudnick, R., and S. Gao, 2003, Composition of the continental crust: *Treatise on geochemistry*, v. 3, p.  
823 1-64, Doi. 10.1016/0016-7037(95)00038-2.

824 Schenk, C., R. Pollastro, and R. Hill, 2006, Natural bitumen resources of the United States: US  
825 Geological Survey Fact Sheet, v. 3133, p. 1-2.

826 Selby, D., and R. A. Creaser, 2005, Direct radiometric dating of hydrocarbon deposits using rhenium-  
827 osmium isotopes: *Science*, v. 308, p. 1293-1295, Doi. 10.1126/science.1111081.

828 Selby, D., R. A. Creaser, K. Dewing, and M. Fowler, 2005, Evaluation of bitumen as a 187Re–187Os  
829 geochronometer for hydrocarbon maturation and migration: a test case from the Polaris  
830 MVT deposit, Canada: *Earth and Planetary Science Letters*, v. 235, p. 1-15, Doi.  
831 10.1016/j.epsl.2005.02.018.

832 Selby, D., R. A. Creaser, and M. G. Fowler, 2007, Re–Os elemental and isotopic systematics in crude oils:  
833 *Geochimica et Cosmochimica Acta*, v. 71, p. 378-386, Doi. 10.1016/j.gca.2006.09.005.

834 Shi, C., J. Cao, J. Bao, C. Zhu, X. Jiang, and M. Wu, 2015, Source characterization of highly mature  
835 pyrobitumens using trace and rare earth element geochemistry: Sinian–Paleozoic paleo-oil  
836 reservoirs in South China: *Organic Geochemistry*, v. 83-84, p. 77-93, Doi.  
837 10.1016/j.orggeochem.2015.03.008.

838 Si, S., 2013, Comparison of Characteristics of Hydrocarbon Accumulation between Bashituo and  
839 Manan Structural Belts in Markit Slope, Tarim Basin, China University of Geoscience  
840 (Wuhan).

841 Smoliar, M. I., R. J. Walker, and J. W. Morgan, 1996, Re-Os ages of group IIA, IIIA, IVA, and IVB iron  
842 meteorites: *Science*, v. 271, p. 1099-1102, Doi. 10.1126/science.271.5252.1099.

843 Stasiuk, L., and L. Snowdon, 1997, Fluorescence micro-spectrometry of synthetic and natural  
844 hydrocarbon fluid inclusions: crude oil chemistry, density and application to petroleum  
845 migration: *Applied Geochemistry*, v. 12, p. 229-241, Doi. 10.1016/S0883-2927(96)00047-9.

846 Su, A., K. Cheng, and W. Jin, 1991, Applications of microscopic fluorescent analysis of source rock  
847 slices on primary migration of petroleum *Petroleum Exploration and Development*, v. 18, p.  
848 19-24.

849 Teinturier, S., J. Pironon, and F. Walgenwitz, 2002, Fluid inclusions and PVTX modelling: examples  
850 from the Garn Formation in well 6507/2-2, Haltenbanken, Mid-Norway: *Marine and*  
851 *Petroleum Geology*, v. 19, p. 755-765, Doi. 10.1016/S0264-8172(02)00055-7.

852 Tian, W., 2005, Burial history of the Kongquehe region in Tarim Basin, Jinlin University 73 p.

853 Visser, W., 1982, Maximum diagenetic temperature in a petroleum source-rock from Venezuela by  
854 fluid inclusion geothermometry: *Chemical Geology*, v. 37, p. 95-101, Doi. 10.1016/0009-  
855 2541(82)90069-9.

856 Wei, G., C. Jia, H. Song, Y. Shi, H. Lu, and Y. Li, 2000, Ordovician Structural - Depositional Model and  
857 Prediction for Profitable Crack Reservoir of Carbonate Rock in Tazhong Area, Tarim: *Acta*  
858 *Sedimentologica Sinica*, v. 18, p. 408-413, Doi. 10.14027/j.cnki.cjxb.2000.03.014.

859 Wenger, L. M., and G. H. Isaksen, 2002, Control of hydrocarbon seepage intensity on level of  
860 biodegradation in sea bottom sediments: *Organic Geochemistry*, v. 33, p. 1277-1292, Doi.  
861 10.1016/S0146-6380(02)00116-X.

862 Wu, L., Y. Liao, Y. Fang, and A. Geng, 2012, The study on the source of the oil seeps and bitumens in the  
863 Tianjingshan structure of the northern Longmen Mountain structure of Sichuan Basin, China:  
864 *Marine and Petroleum Geology*, v. 37, p. 147-161, Doi. 10.1016/j.marpetgeo.2012.05.011.

865 Xiao, H., J. Zhao, H. Yang, Z. Cai, Y. Zhu, L. Huang, and N. Zhang, 2012, Fluid Inclusion and Micro-FTIR  
866 Evidence for Hydrocarbon Charging Fluid Evolution of the Ordovician Reservoir of  
867 Halahatang Depression, the Tarim Basin: *Earth Science-Journal of China University of*  
868 *Geosciences*, v. 37, p. 163-173, Doi. 10.3799/dqkx.2012.S1.016.

869 Xiao, H., J. Zhao, Y. Zhu, and Y. Li, 2013, Geochemical Tracking on Hydrocarbon Accumulation Periods  
870 of Ordovician in Hanilcatam Sag, Tarim Basin: *Xinjiang Petroleum Geology*, v. 34, p. 465-468.

871 Xiao, X., and M. Tang, 2003, The Tarim Basin becoming the biggest onshore natural gas production  
872 area in China: *Natural Gas Geoscience* v. 14, p. 35-38.

873 Xiao, Z., M. Li, S. Huang, T. Wang, B. Zhang, R. Fang, K. Zhang, Z. Ni, Q. Zhao, and D. Wang, 2016, Source,  
874 oil charging history and filling pathways of the Ordovician carbonate reservoir in the  
875 Halahatang Oilfield, Tarim Basin, NW China: *Marine and Petroleum Geology*, v. 73, p. 59-71,  
876 Doi. 10.1016/j.marpetgeo.2016.02.026.

877 Xu, G., C. Lin, Y. Liu, and Q. Sun, 2016, Evolution of Palaeo Uplift and Its Controlling on Sedimentation  
878 of Kapushaliang Group of Early Cretaceous in Western Tabei Uplift: *Earth Science*, v. 41, p.  
879 619-632, Doi. 10.3799/dqkx.2016.051.

880 Xu, X., Q. Zhou, and L. Zhang, 2004, Oil and gas reserves and their distribution in Tarim Basin: *Oil &  
881 Gas Geology*, v. 25, p. 300-303.

882 Yang, C., Z. Wang, B. P. Hollebone, C. E. Brown, and M. Landriault, 2009, Characteristics of bicyclic  
883 sesquiterpanes in crude oils and petroleum products: *Journal of Chromatography A*, v. 1216,  
884 p. 4475-4484, Doi. 10.1016/j.chroma.2009.03.024.

885 Zhang, G., W. Zhao, H. Wang, H. Li, and L. Liu, 2007a, Multicycle tectonic evolution and composite  
886 petroleum systems in the Tarim Basin: *Oil & Gas Geology*, v. 28, p. 653-663.

887 Zhang, P., S. Zhang, and Y. He, 1990, Issues on oil classification *Oil & Gas Storage and Transportation*, v.  
888 9, p. 74-77.

889 Zhang, S., and H. Huang, 2005, Geochemistry of Palaeozoic marine petroleum from the Tarim Basin,  
890 NW China: Part 1. Oil family classification: *Organic Geochemistry*, v. 36, p. 1204-1214, Doi.  
891 10.1016/j.orggeochem.2005.01.013.

892 Zhang, W., S. Zhu, S. He, and Y. Wang, 2015, Screening of oil sources by using comprehensive two-  
893 dimensional gas chromatography/time-of-flight mass spectrometry and multivariate  
894 statistical analysis: *Journal of Chromatography A*, v. 1380, p. 162-170, Doi.  
895 10.1016/j.chroma.2014.12.068.

896 Zhang, X., Y. Duan, J. He, B. Wu, and L. Xu, 2011, Geochemical Characteristics of Crude Oil in Lower  
897 Part of Yanchang Formation and Correlation of Oil Source in Huaqing Area of Ordos Basin:  
898 *Natural Gas Geoscience* v. 22, p. 866-873.

899 Zhang, Y., Z. Horst, K. Liu, and X. Luo, 2007b, K-Ar isotopic dating of authigenic illite and its  
900 application to the investigation of hydrocarbon accumulation history of the Silurian  
901 bitumious sandstone reservoirs in the Tazhong uplift, Tarim basin: *Oil & Gas Geology*, v. 28, p.  
902 166-174.

903 Zhang, Y., Z. Horst, A. Todd, K. Liu, and X. Luo, 2004, K-Ar dating of authigenic illite and its  
904 applications to study of oil-gas charging histories of typical sandstone reservoirs, Tarim  
905 Basin, Northwest China: *Earth Science Frontiers* v. 4, p. 637-648.

906 Zhang, Y., and X. Luo, 2011, K-Ar dating of authigenic illites and hydrocarbon accumulation history of  
907 the Silurian bitumious sandstons reservoirs in Yingmai area, Tarim Basin: *Petroleum  
908 Exploration and Development*, v. 38, p. 203-210.

909 Zhao, J., Q. Li, Q. Wang, W. Pang, B. Shi, and J. Luo, 2004, On the formation and distribution of mid-  
910 large oil and gas fields in the Tarim Basin: *Journal of Northwest University (Nature Science  
911 Edition)*, v. 34, p. 212-217, Doi. 10.16152/j.cnki.xdxzbz.2004.02.022.

912 Zhu, G., H. Yang, Y. Zhu, L. Gu, Y. Lu, J. Su, B. Zhang, and Q. Fan, 2011, Study on petroleum geological  
913 characteristics and accumulation of carbon reservoirs in Hanilcatam area, Tarim Basin: *Acta  
914 Petrologica Sinica*, v. 27, p. 827-844.

915 Zhu, G., S. Zhang, K. Liu, H. Yang, B. Zhang, J. Su, and Y. Zhang, 2013a, A well-preserved 250 million-  
916 year-old oil accumulation in the Tarim Basin, western China: Implications for hydrocarbon  
917 exploration in old and deep basins: *Marine and Petroleum Geology*, v. 43, p. 478-488, Doi.  
918 10.1016/j.marpetgeo.2012.12.001.

919 Zhu, G., S. Zhang, J. Su, H. Huang, H. Yang, L. Gu, B. Zhang, and Y. Zhu, 2012, The occurrence of ultra-  
920 deep heavy oils in the Tabei Uplift of the Tarim Basin, NW China: *Organic Geochemistry*, v. 52,  
921 p. 88-102, Doi. 10.1016/j.orggeochem.2012.08.012.

922 Zhu, G., S. Zhang, J. Su, S. Meng, H. Yang, J. Hu, and Y. Zhu, 2013b, Secondary accumulation of  
923 hydrocarbons in Carboniferous reservoirs in the northern Tarim Basin, China: *Journal of  
924 Petroleum Science and Engineering*, v. 102, p. 10-26, Doi. 10.1016/j.petrol.2013.01.005.

925 Zhu, G., S. Zhang, J. Su, B. Zhang, H. Yang, Y. Zhu, and L. Gu, 2013c, Alteration and multi-stage  
926 accumulation of oil and gas in the Ordovician of the Tabei uplift, Tarim Basin, NW China:  
927 implications for genetic origin of the diverse hydrocarbons: *Marine and Petroleum Geology*, v.

928 46, p. 234-250, Doi. 10.1016/j.marpetgeo.2013.06.007.  
929 Zumberge, J. E., 1987, Prediction of source rock characteristics based on terpane biomarkers in crude  
930 oils: A multivariate statistical approach: *Geochimica et Cosmochimica Acta*, v. 51, p. 1625-  
931 1637, Doi. 10.1016/0016-7037(87)90343-7.  
932

933 **Author's vita**

934 **Xiang Ge**

935 Key Laboratory of Tectonics and Petroleum Resources (China University of  
936 Geosciences), Ministry of Education, Wuhan, 430074, China; 388 Lumo Road, Hongshan  
937 District, Wuhan City, Hubei Province, China.

938 [xiangge89@126.com](mailto:xiangge89@126.com)

939 Xiang Ge is an Associate Professor at the China University of Geoscience (Wuhan)  
940 (CUG). He received his B.Sc., M.Sc. and Ph.D from China University of Geoscience  
941 (Wuhan). As an joint Ph.D student of CUG and Durham University, his research is  
942 focusing on the petroleum geology of the Sichuan and Tarim Basin applying hydrocarbon  
943 Re-Os isotope, organic geochemistry, structural and tectonic analyses.

944 **Chuanbo Shen (\*Corresponding author)**

945 Key Laboratory of Tectonics and Petroleum Resources (China University of  
946 Geosciences), Ministry of Education, Wuhan, 430074, China; 388 Lumo Road,  
947 Hongshan District, Wuhan City, Hubei Province, China.

948 [cugshen@126.com](mailto:cugshen@126.com)

949 Chuanbo Shen (Corresponding author) is currently a professor in the Faculty of Earth  
950 Resources at the China University of Geosciences (Wuhan). He received his B.Sc.,  
951 M.Sc., and Ph.D. from China University of Geoscience (Wuhan). He also completed  
952 postdoctoral research in Technische Universität Bergakademie Freiberg, Germany. His  
953 present research interests are low-temperature thermochronology, tectonic-thermal

954 evolution and hydrocarbon geochronology.

955 **David Selby**

956 Department of Earth Sciences, Durham University, Durham, DH1 3LE, UK

957 [david.selby@durham.ac.uk](mailto:david.selby@durham.ac.uk)

958 David Selby is a Professor of Earth Sciences at Durham University, UK. He received a  
959 bachelor's degree in geology from Southampton University, UK and Ph.D. degree from  
960 the University of Alberta, Canada. He also carried out his postdoctoral research at the  
961 University of Alberta. His research focuses on the Earth Science disciplines of economic  
962 geology, petroleum geoscience and paleoclimate / oceanography, principally through the  
963 application and development of the novel, state-of-the-art, rhenium-osmium radio isotope  
964 methodology.

965 **Martin Feely**

966 Earth and Ocean Sciences, School of Natural Sciences, National University of Ireland,  
967 Galway, Ireland

968 [martin.feely@nuigalway.ie](mailto:martin.feely@nuigalway.ie)

969 Martin Feely, BSc., MSc., PhD is an emeritus Professor of Earth and Ocean Sciences in  
970 the School of Natural Sciences, National University of Ireland, Galway. He is Adjunct  
971 Professor of Geological and Environmental Sciences at James Madison University  
972 (JMU), Virginia, USA. He has authored/co-authored over 200 scientific articles and  
973 papers. His research has focused on fluid inclusion studies, methods and applications for  
974 the global mineral and oil research and exploration sectors.

975 **Guangyou Zhu**

976 Research Institute of Petroleum Exploration and Development, PetroChina, 20 Xueyuan  
977 Road, Haidian District, Beijing 100083, China;

978 [zhuguangyou@petrochina.com.cn](mailto:zhuguangyou@petrochina.com.cn)

979 Guangyou Zhu is now a senior expert of geology and geochemistry at the Research  
980 Institute of Petroleum Exploration and Development, PetroChina. He received his B.Sc.  
981 and Ph.D. degree from the China University of Petroleum (Huadong). His research  
982 interests include source rock formation, petroleum accumulation, thermochemical sulfate  
983 reduction, and deep oil and gas phase.

984

### 985 **Figure captions**

986 Fig. 1. (A) Location of the Tarim Basin, China. (B) Structural unit distribution of the  
987 Tarim Basin. (C) Regional map of the Halahatang depression, Yingmaili Uplift, Luntai  
988 Uplift, Lunnan Uplift and the Northern Depression (Substantially modified from (Zhu et  
989 al., 2012)). Also shown are the sample locations for the Re-Os analysis of this study and  
990 the illite K-Ar analysis (Zhang and Luo, 2011; Zhu et al., 2012). The dash line A-A'  
991 shows the location of the cross section profile presented in Figure 8.

992

993 Fig. 2. Combined Stratigraphic sequences, hydrocarbon system and tectonic events in the  
994 north Tarim Basin. Substantially modified after Chang et al., 2013a; Lin et al., 2015 and  
995 Zhang and Huang, 2005

996

997 Fig. 3. Photomicrographs of (A) an example of a liquid-rich, two-phase (L+V; L>V)  
998 aqueous inclusion (~10 microns in longest dimension) in sample Ha9 and (B) an example  
999 of a two-phase hydrocarbon bearing fluid inclusion (~10 microns in longest dimension)  
1000 in sample Ha9. (C, D) examples of hydrocarbon bearing fluid inclusions under

1001 fluorescent light in sample Ha9.

1002

1003 Fig. 4. GC,  $m/z$  191 and  $m/z$  217 mass chromatogram of the oil samples (Ha9, Ha11,  
1004 Ha701, XK4-3 and Ha15-2) in Halahatang oilfield, northern Tarim Basin.

1005

1006 Fig. 5. (A). plots of Pristane/ $nC_{17}$  and Phytane/ $nC_{18}$  alkane ratios for sampled oils. (B)  
1007 Histogram of the Pr/Ph ratios for sampled oils. (C) Distribution of the tricyclic terpanes  
1008 (ratios of  $C_{23}TT/C_{21}TT$ ,  $C_{23}TT/C_{24}TT$ ,  $C_{19}TT/C_{23}TT$  and  $C_{24}TET/C_{26}TT$ ) for the samples  
1009 oils. (D) Histogram of the Ts/Ts+Tm ratio for the sampled oils. (E) Plots of  
1010  $C_{29}\alpha\alpha/20S/(20S+20R)$  (~0.43) and  $C_{29}\beta\beta/(\beta\beta+\alpha\alpha)$  (~0.57) of the sampled oils. (F)  
1011 Histogram of the  $C_{29}Nor_{25}H/C_{30}H$  ratio for the sampled oils.

1012

1013 Fig. 6. (A) A Th frequency distribution histogram of aqueous, coeval (with hydrocarbon-  
1014 bearing fluid inclusions) aqueous and hydrocarbon-bearing fluid inclusions in sample  
1015 Ha9. (B) A Th-salinity bivariate plot of aqueous fluid inclusions in sample Ha9. (C) A  
1016 bivariate plot of Fv (at 20°C) Th for three selected hydrocarbon bearing fluid inclusions  
1017 from sample Ha9. Seven oil types after (Bourdet et al., 2008) are also plotted for  
1018 reference indicating that the fluid inclusion hosted oils in sample Ha9 similar in  
1019 composition to N. America volatile oils (NA = North America).

1020

1021 Fig. 7. (A) A burial history temperature-time plot for the Halahatang oilfield, showing the  
1022 key time for oil migration and or accumulation. (B) A Th frequency distribution  
1023 histogram for aqueous fluid inclusions coeval with hydrocarbon-bearing fluid inclusions

1024 in sample Ha 9. (C) A P-T plot of isopleths and isochores for aqueous and hydrocarbon  
1025 bearing fluid inclusions in Ha9. Isopleths and isochores of the hydrocarbon fluids are  
1026 determined using PIT modeling (Montel, 1993; Pironon, 2004), whereas isopleths and  
1027 isochores for the aqueous fluids were generated using (Duan and Mao, 2006). The dash-  
1028 point lines: coeval aqueous fluid inclusions (PI with AI). The dash lines: non-coeval  
1029 aqueous fluid inclusions (AI). The solid lines: three hydrocarbon bearing fluid inclusions  
1030 (PI)(plotted in Fig 5C) and are coeval with the aqueous fluid inclusions. Intersections  
1031 between the coeval isochores yield estimates of true fluid trapping temperatures and  
1032 pressures. See text for discussion.

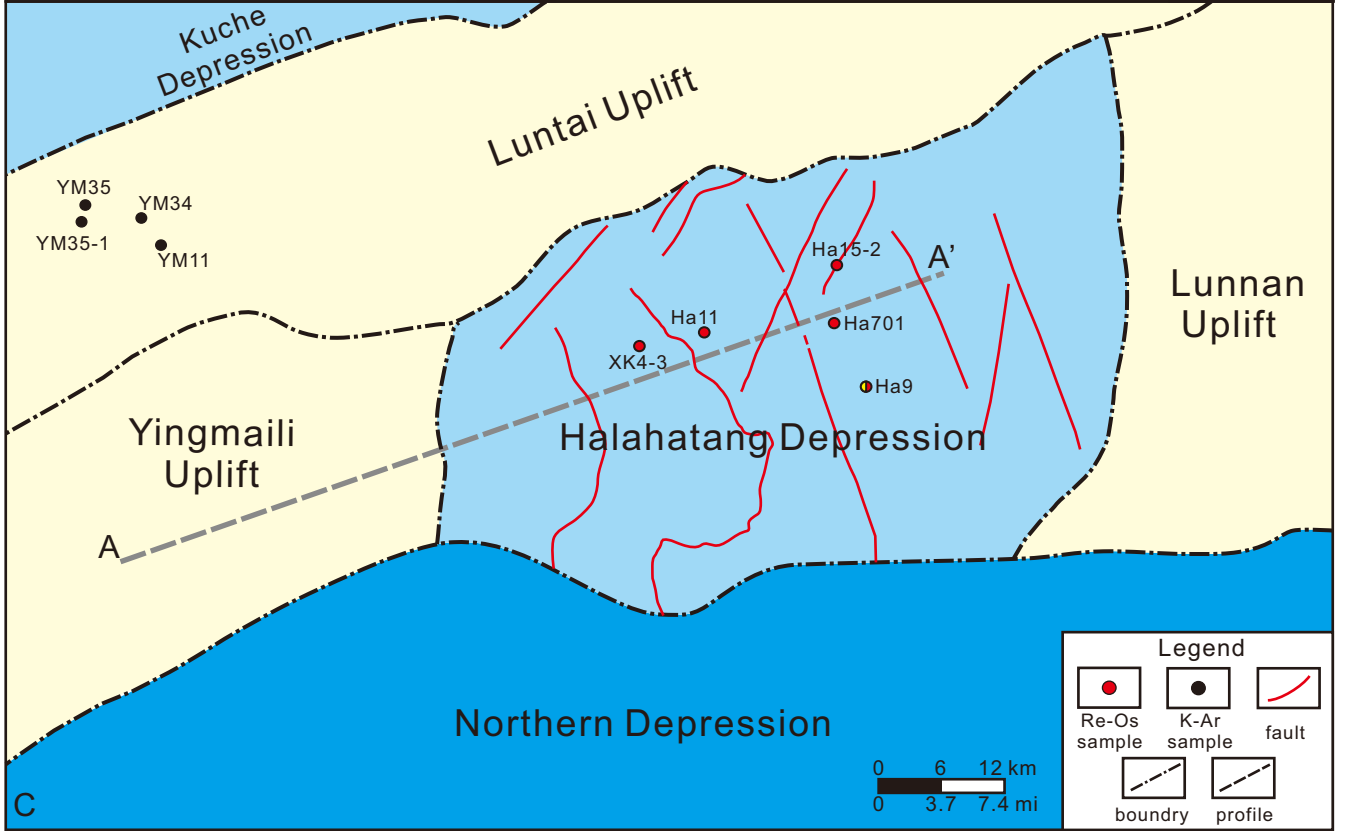
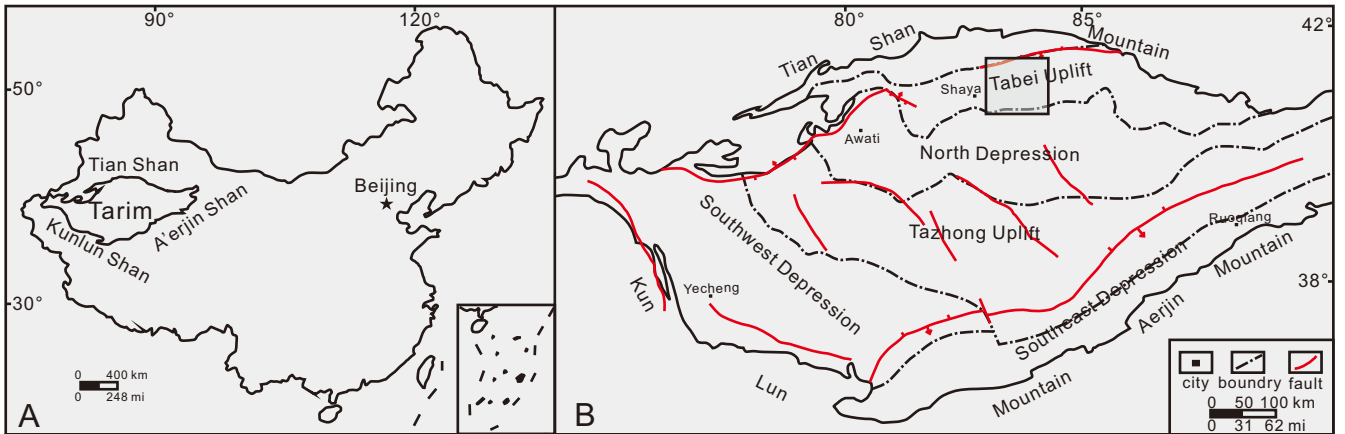
1033

1034 Fig. 8. Re-Os isochron plot of all oil samples Ha9, Ha9rpt, Ha11, Ha701, XK4-3. Data-  
1035 point ellipses shown at the 2-sigma level absolute uncertainty. The Re-Os data for all  
1036 samples, except Ha15-2 and Ha15-2rpt, yield a Re-Os date of  $285 \pm 48$  Ma, with an  
1037 initial  $^{187}\text{Os}/^{188}\text{Os}$  of  $1.08 \pm 0.20$  (MSWB = 6.1). Ha9rpt and Ha15-2rpt are repeated  
1038 analysis of samples Ha9 and Ha15-2.

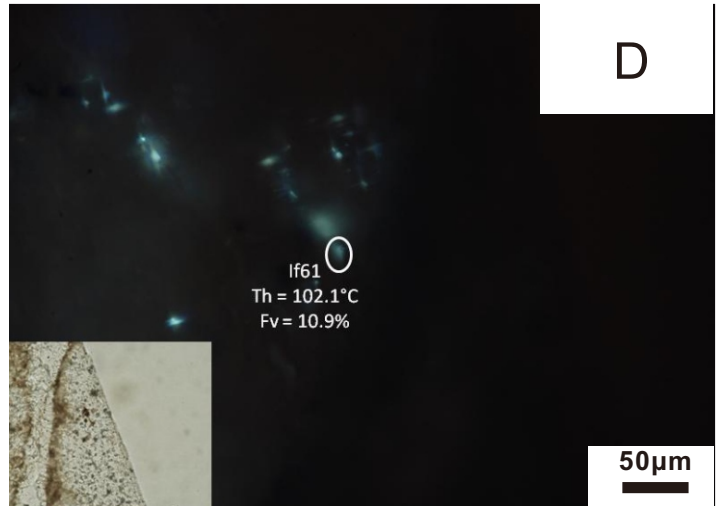
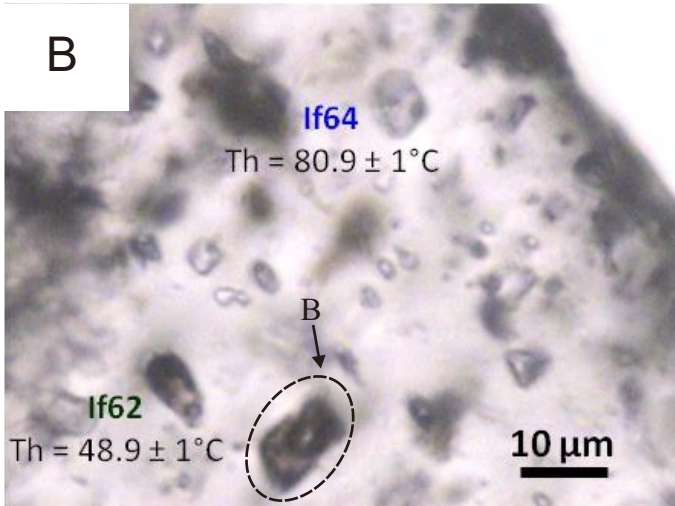
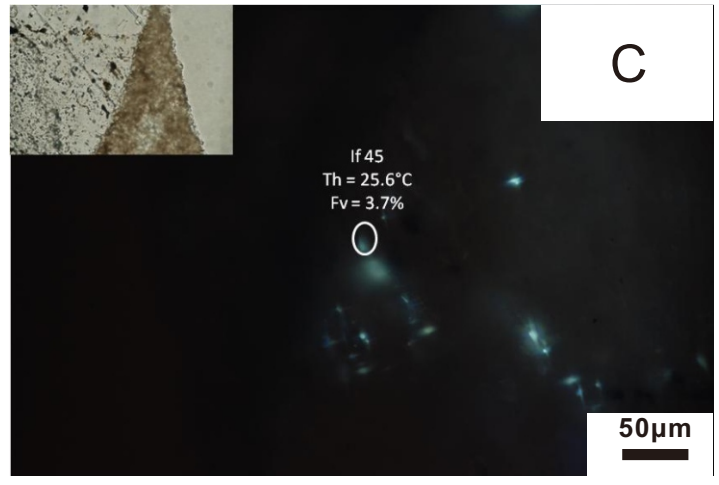
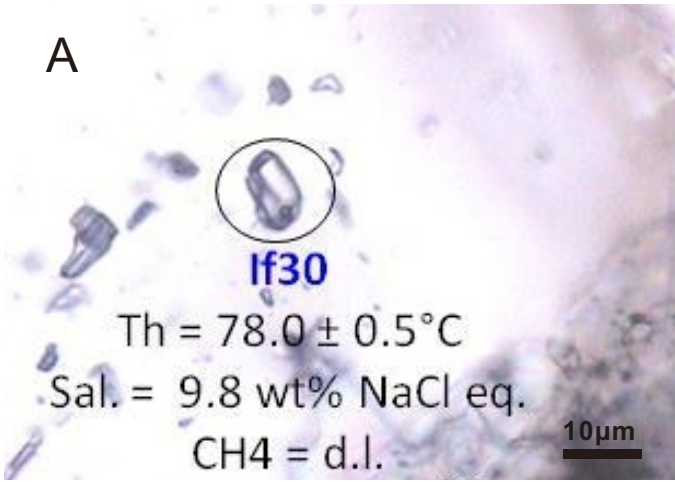
1039

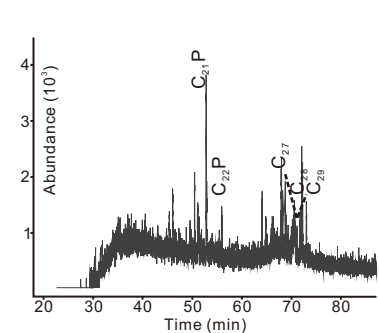
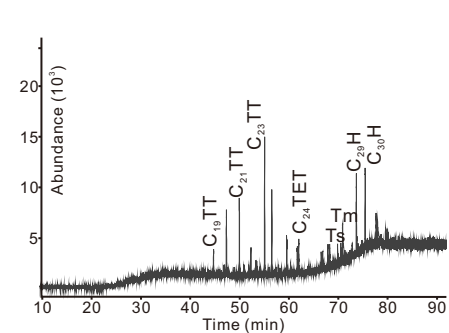
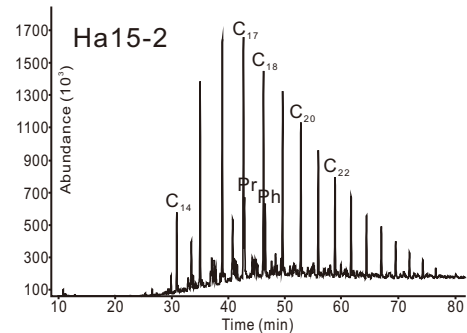
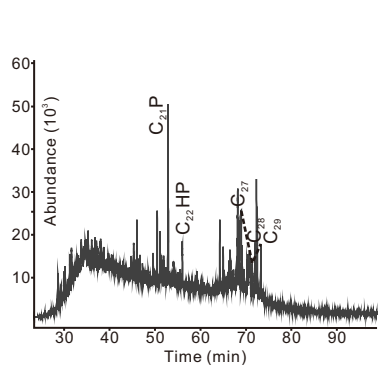
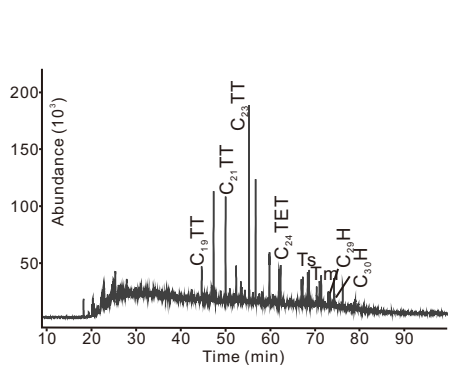
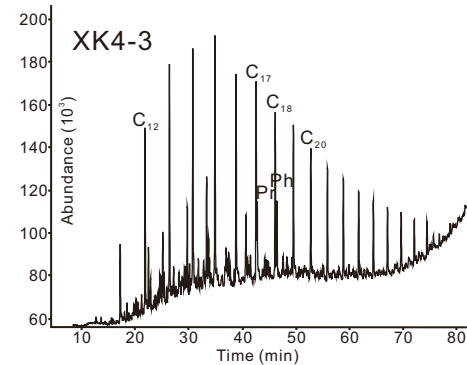
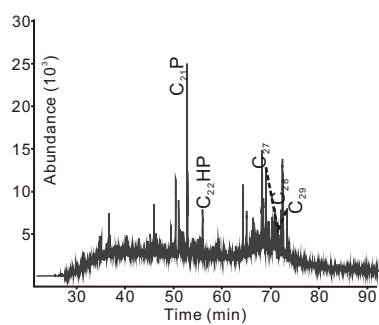
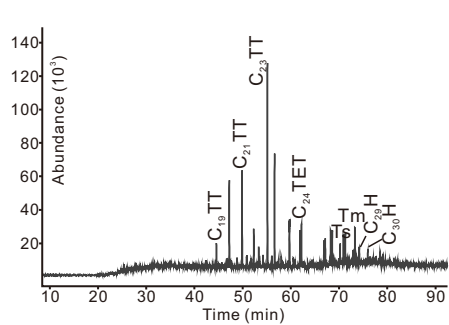
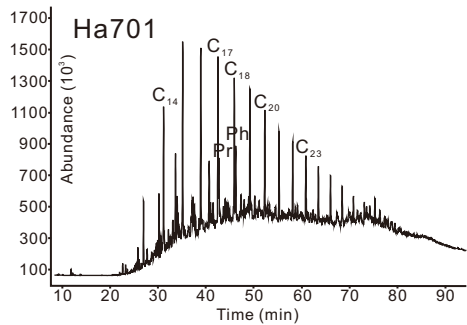
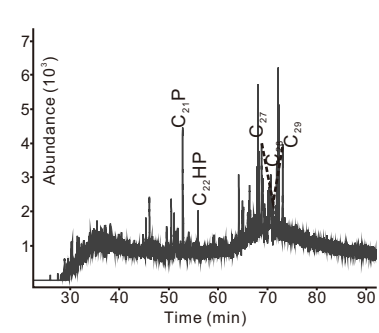
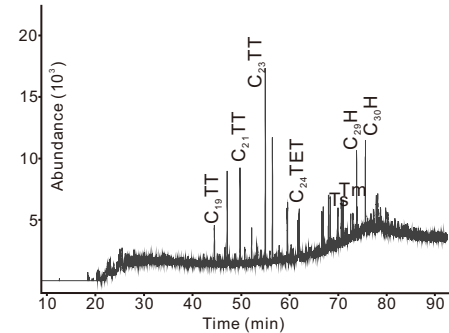
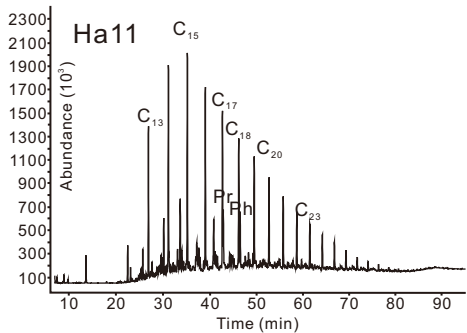
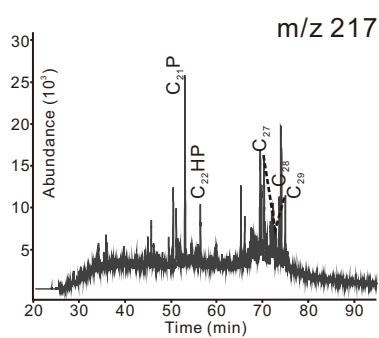
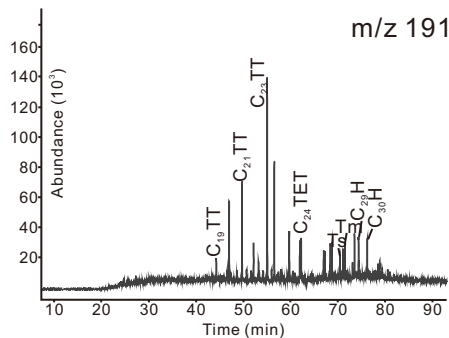
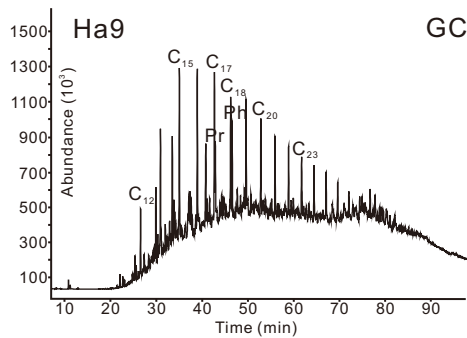
1040 Fig. 9. Petroleum evolution model for the Halahatang oilfield, northern Tarim Basin. (A)  
1041 Halahatang depression during the Late Silurian. (B). Oil generation during the Early  
1042 Permian. (C) Oil migration/accumulation process during the Late Permian to Early  
1043 Triassic. (D) Present day configuration of the Halahatang oilfield after continuous  
1044 sedimentation since the Late Triassic. See text for discussion.

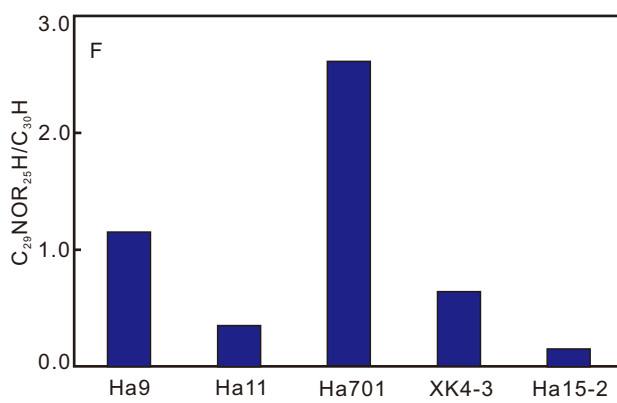
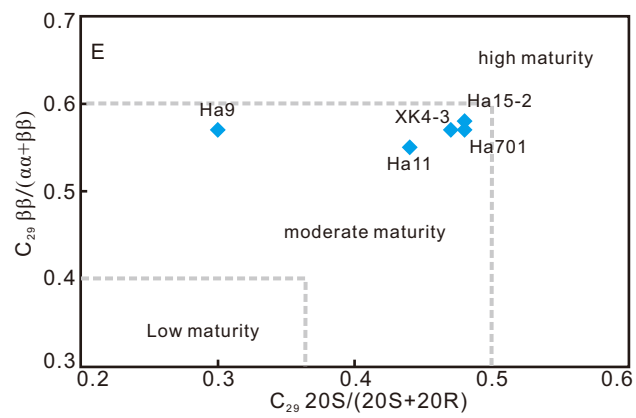
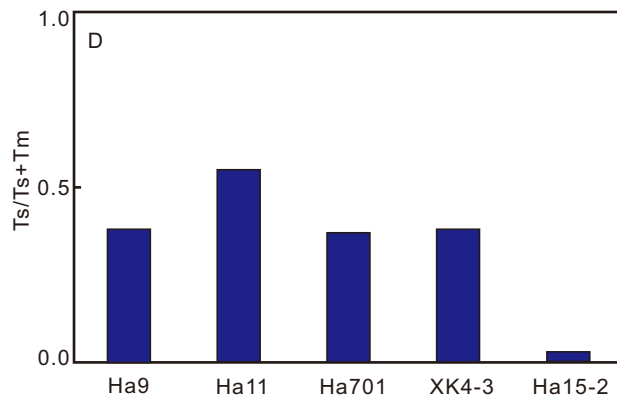
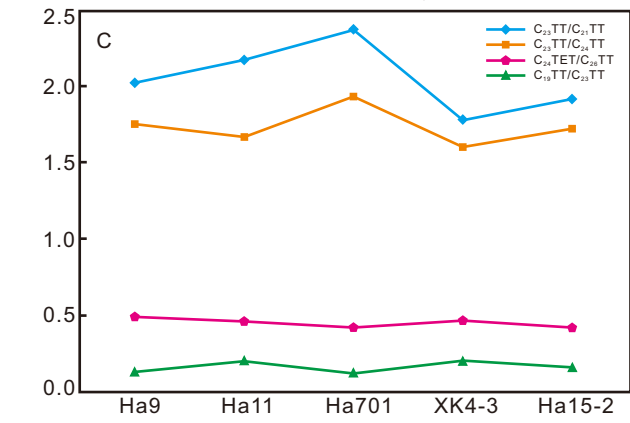
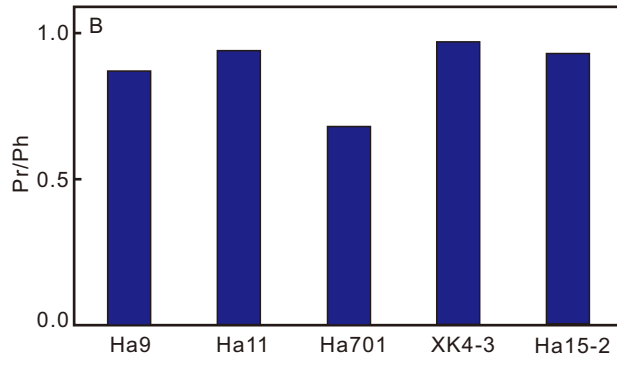
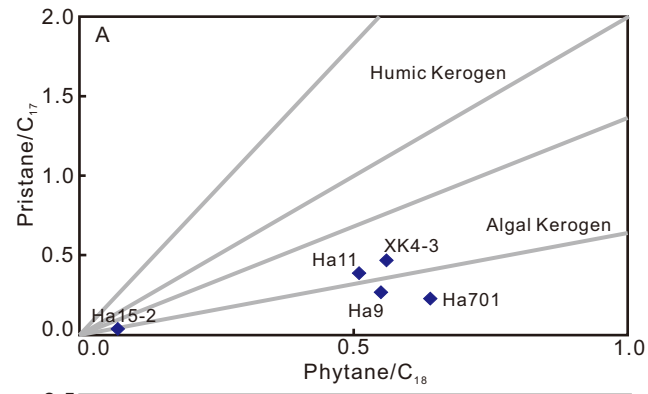
1045

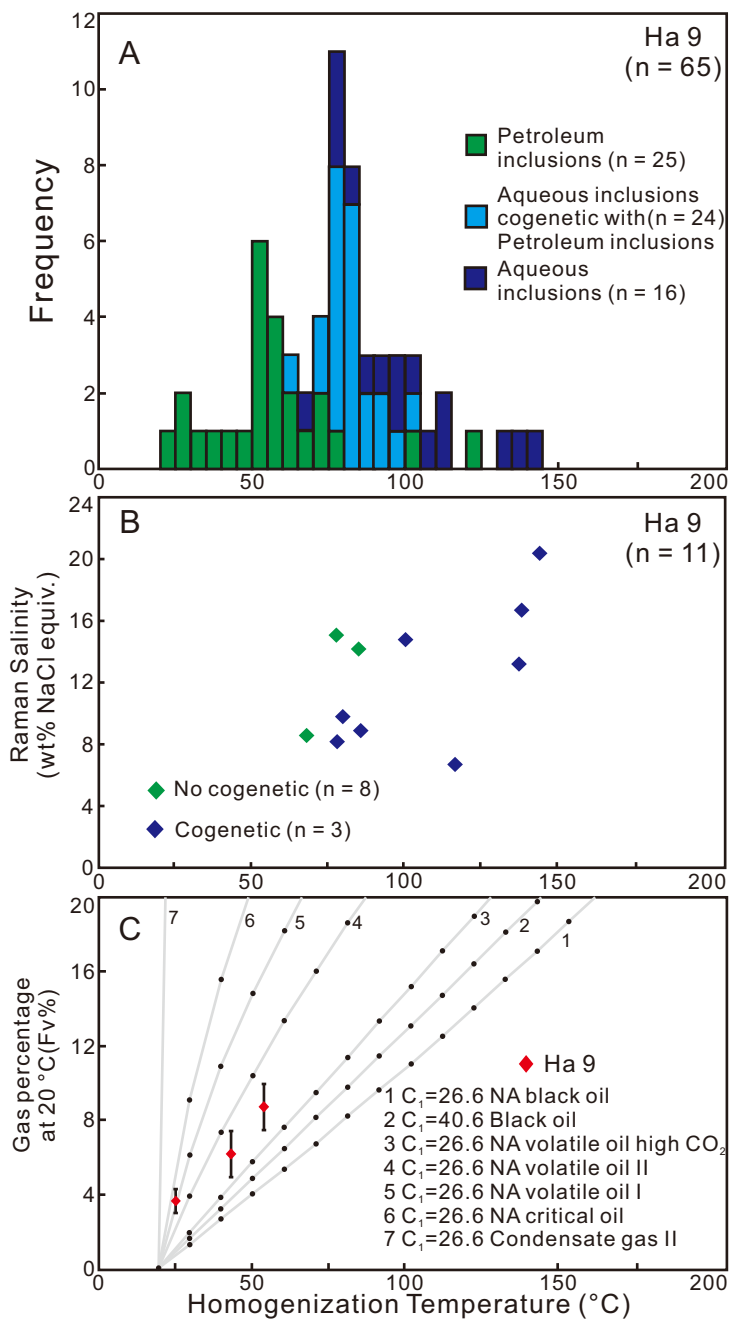


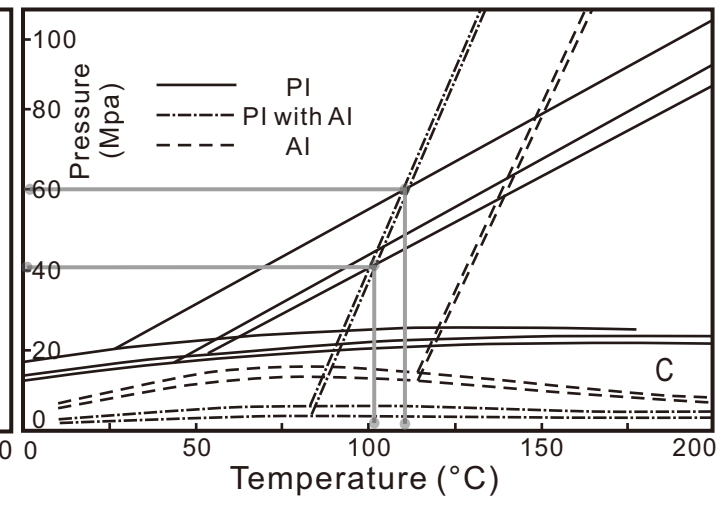
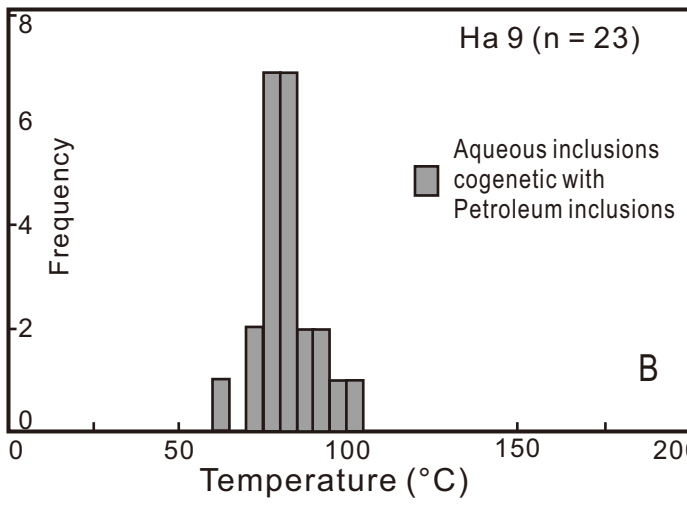
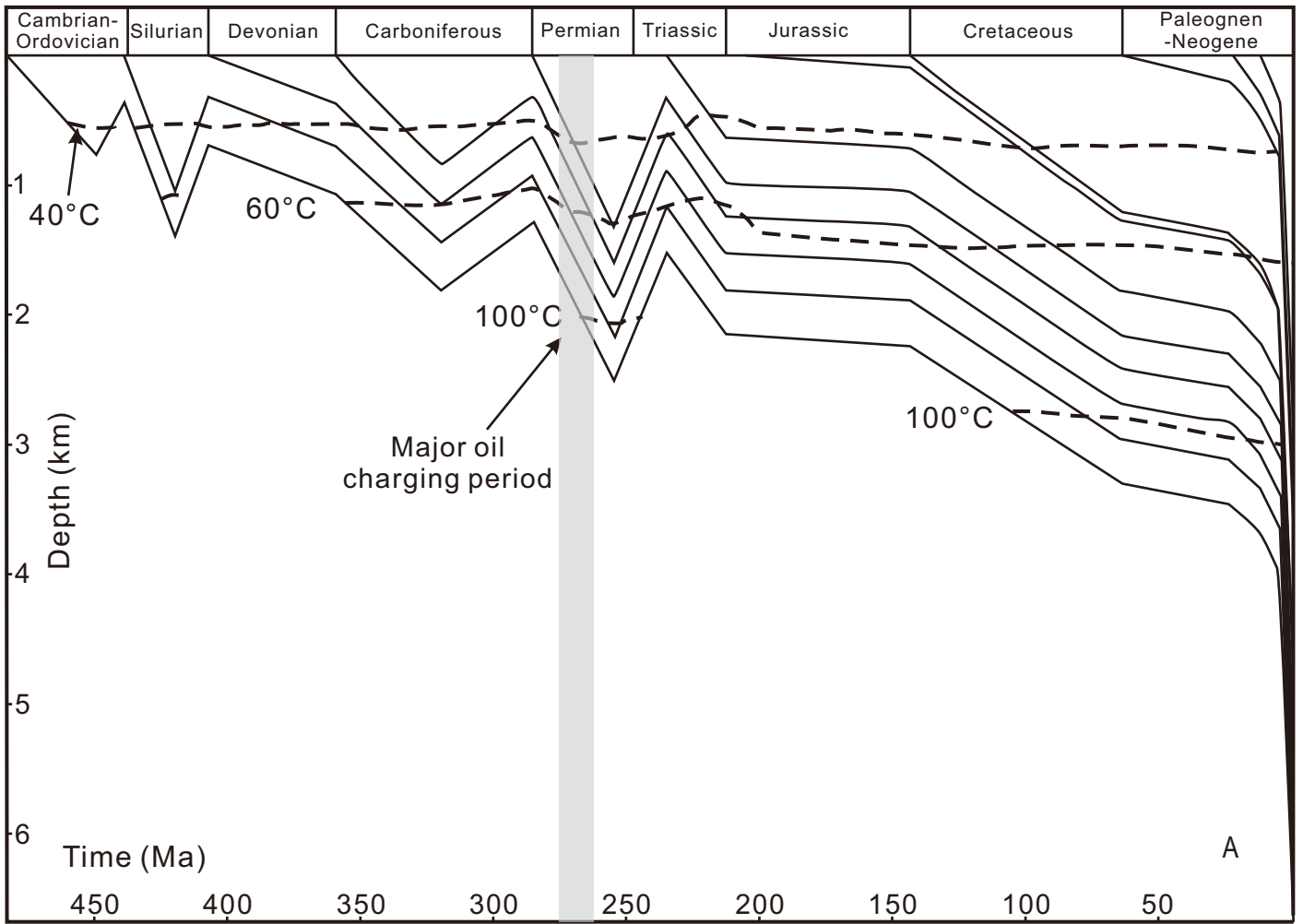
Period	Formation	Lithology	Thickness (m)	Petroleum System	Tectonic Cycle	
Quaternary			100-200		Himalayan Movement	
	2.5	Xiyu				
Neogene	Kuche		2000 - 4000			
	Kangcun					
	23	Jidike				
Paleogene	Suweiyi		100-500			
	65	Kumugeliemu				
Cretaceous	Kapushaliang		200-600			
Jurassic			100-300			Yanshan Movement
Triassic	Halahatang		400-600	reservoir		Indosinian Movement
	Akekule					
Permian	Ketuler		300-500			
	252	Shajingzi				
	Kaipaizileike					
Carboniferous	Kupukuziman		300-800		Hercynian Movement	
	299	Nanmin				
Devonian	Xiaohaizi		300-800			
	359	Kalashayi				
	Bachu					
Devonian	Donghetang		0-300	reservoir		
Silurian	Keziertage		0-1000			
	444	Yimugantanwu				
	Tataaiertage					
Ordovician	Kepingtage		500 - 2000			
	Sangtamu					
	Lianglitage					
	Qiaerbake					
	485	Yijianfang				
Cambrian	Yingshan				Caledonian Movement	
	Penglaibai					
	Qiulitagexia					
	Awatage					
	542	Shayilike				
Neo-proterozoic	Wusonggeer		200 - 1000	reservoir		
	Xiaoerbulake			source		
	Yuertusi					
	Qigebulake					
	650	Sugaitebulaike				

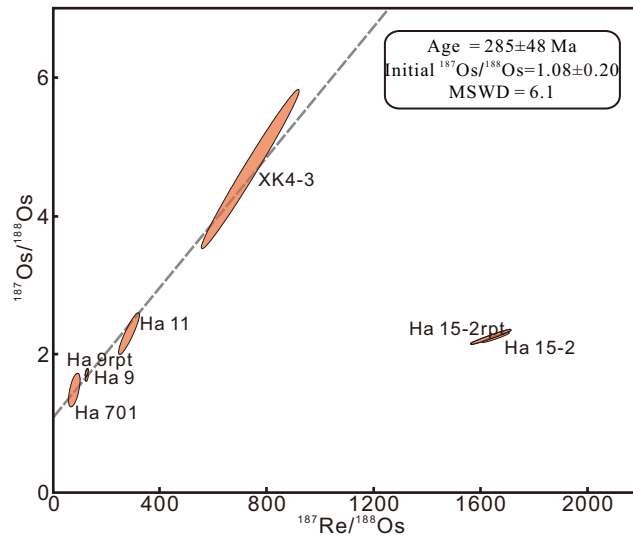












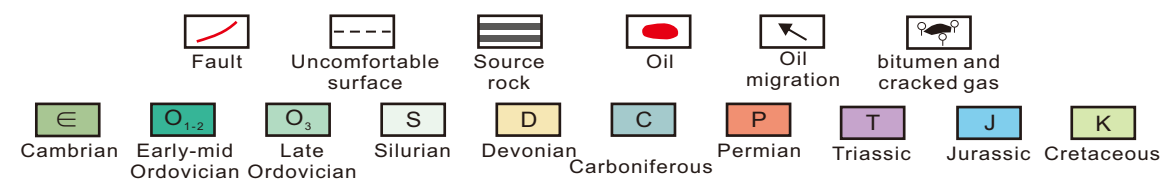
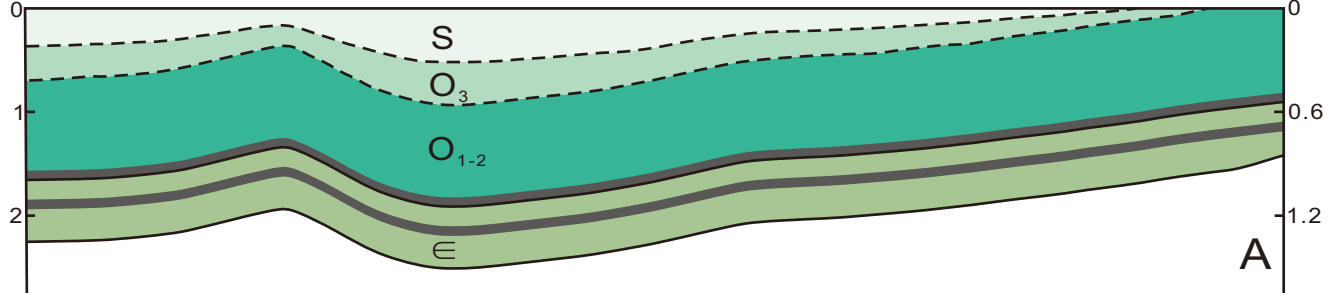
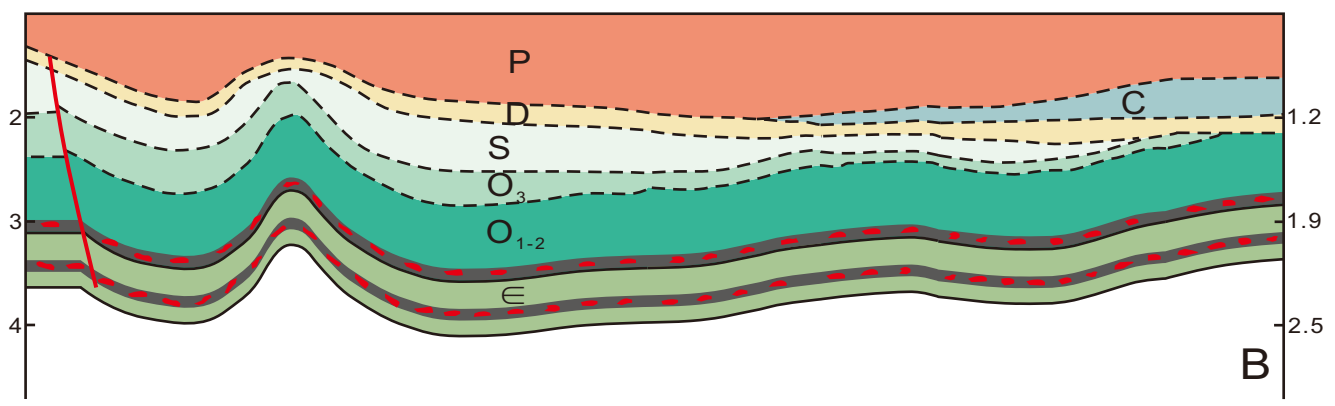
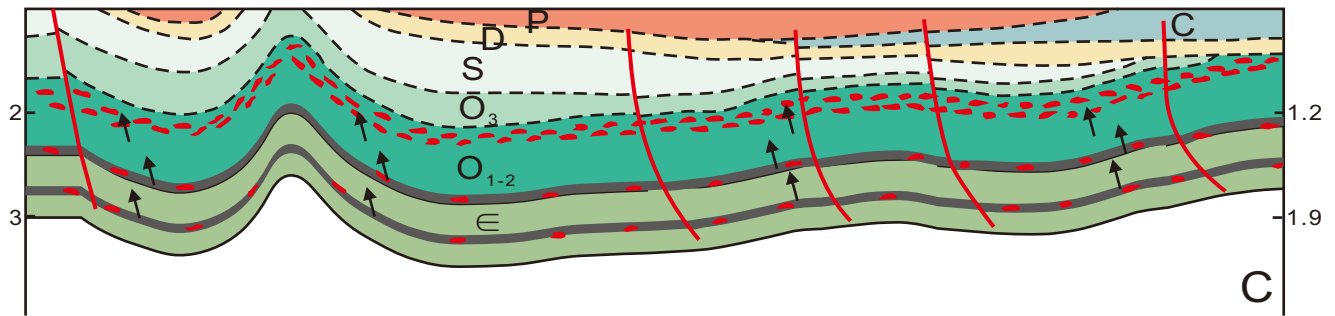
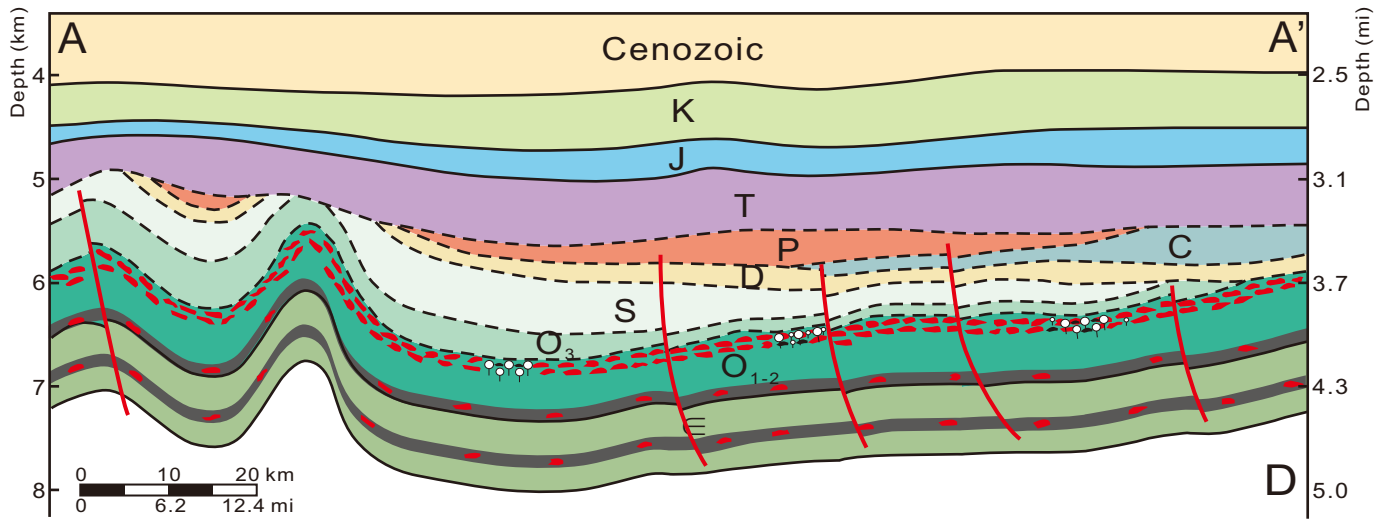


Table 1. Physical properties, sulfur content and component of the oil from the halahatang oilfield.

Well name	Depth (m)	Formation Name	Density (g/cm <sup>3</sup> )		Viscosity (mPa·s, 50 °C)	API vaule	Wax (%)	Sulfur (%)	Saturate (%)	Aromatic (%)	Resin (%)	Asphaltene (%)
			20 °C	50 °C								
Ha 9	6598-6710	Ordovician Yijianfang	0.879	0.859	6.92	29.48	3.80	0.84	57.33	10.00	6.67	23.33
Ha 11	6658-6748	Ordovicia Yijianfang	0.833	0.812	2.62	38.37	6.10	0.50	64.67	14.33	3.67	14.33
Ha 15-2	6559-6598	Ordovician Yijianfang	0.844	0.822	3.15	36.15	8.60	0.63	56.00	18.00	4.33	18.67
Ha 701	6557-6618	Ordovician Yijianfang	1.011	0.992	342.3	8.46	/	0.67	46.92	13.36	3.42	33.56
XK4-3	6834-6850	Ordovician Yijianfang	0.88	0.86	7.96	29.30	5.90	0.59	55.49	26.55	5.24	3.56

/: Not measured

Table 2. The biomarker parameters of the oil samples from Halahatang oilfield.

Sample name	Pr/nC <sub>17</sub>	Ph/nC <sub>18</sub>	Pr/Ph	C <sub>23</sub> TT/C <sub>21</sub> TT	C <sub>23</sub> TT/C <sub>24</sub> TT	C <sub>19</sub> TT/C <sub>23</sub> TT	C <sub>24</sub> TET/C <sub>26</sub> TT	Ts/(Ts+Tm)	GAM/C <sub>30</sub> H
Ha9	0.27	0.55	0.87	2.02	1.75	0.13	0.49	0.38	0.19
Ha11	0.39	0.51	0.94	2.17	1.67	0.20	0.46	0.55	0.12
Ha701	0.23	0.64	0.68	2.37	1.93	0.12	0.42	0.37	0.15
XK4-3	0.47	0.56	0.97	1.78	1.60	0.20	0.47	0.38	0.05
Ha15-2	0.04	0.07	0.93	1.91	1.72	0.16	0.42	0.03	0.07
	C <sub>30</sub> DH/ C <sub>30</sub> H	C <sub>29</sub> NOR <sub>25</sub> H/ C <sub>30</sub> H	C <sub>21</sub> P/C <sub>22</sub> HP	C <sub>27</sub> R (%)	C <sub>28</sub> R (%)	C <sub>29</sub> R (%)	C <sub>29</sub> ααα20S/(20S+20R)	C <sub>29</sub> ββ/(ββ+αα)	
Ha9	0.10	1.15	3.12	56.69	7.56	35.75	0.30	0.57	
Ha11	0.03	0.35	2.98	37.40	20.07	42.53	0.44	0.55	
Ha701	0.13	2.61	4.20	65.37	7.02	27.60	0.48	0.57	
XK4-3	0.10	0.64	5.69	49.64	15.96	34.39	0.47	0.57	
Ha15-2	0.10	0.15	4.15	42.20	22.70	35.11	0.48	0.58	

Table 3. Summary of petrographic observations, microthermometry, Laser Raman Microspectroscopy and CSLM results of aqueous and oil-bearing inclusions for sample Ha9.

Sample Name	Inclusion No.	FI types	types	Th (°C)	Error (°C)	Raman Salinity wt% (NaCl aq.)	Raman Salinity (molal)	CH <sub>4</sub> (molal)	Bulk volume (µm <sup>3</sup> )	Bubble volume (µm <sup>3</sup> )	Fv at 20°C (%)	Relative error %
Ha 9-1A	42	2-phase L-V oil	Calcite cement	52.8	2							
Ha 9-1A	43	2-phase L-V oil	Calcite cement	52.6	1							
Ha 9-1A	44	2-phase L-V aqueous	Calcite cement	98.1	0.2	14.6	3.02	0.1				
Ha 9-1A	45	2-phase L-V oil	Calcite cement	25.6	0.5				94.7	3.5	3.7	17
Ha 9-1B	45b	2-phase L-V oil	Calcite cement	n.m					32.6	1.8	5.1	49
Ha 9-1B	46	2-phase L-V aqueous	Calcite cement	85.8	2							
Ha 9-1B	47	2-phase L-V oil	Calcite cement	25.1	0.3							
Ha 9-1B	48	2-phase L-V aqueous	Calcite cement	71.7	0.3							
Ha 9-1B	49	2-phase L-V oil	Calcite cement	57.2	0.2							
Ha 9-1B	50	2-phase L-V aqueous	Calcite cement	86.7	2							
Ha 9-1B	68	2-phase L-V aqueous	Calcite cement	83.2	0.2	14.2	2.88	0.017-0.026				
Ha 9-1B	69	1-phase L aqueous	Calcite cement			18.6	4.04					
Ha 9-1C	51	2-phase L-V oil	Calcite cement	54.2	0.2							
Ha 9-1C	52	2-phase L-V oil	Calcite cement	24.6	0.3							
Ha 9-1C	53	2-phase L-V oil	Calcite cement	29.2	0.3							
Ha 9-1C	54	2-phase L-V oil	Calcite cement	37	0.2							
Ha 9-1C	55	2-phase L-V aqueous	Calcite cement	83.8	1							
Ha 9-1C	56	2-phase L-V aqueous	Calcite cement	91.6	2							
Ha 9-1C	57	2-phase L-V aqueous	Calcite cement	107.1	2							
Ha 9-1C	58	2-phase L-V aqueous	Calcite cement	77	1							
Ha 9-1C	59	2-phase L-V aqueous	Calcite cement	76.1	1	15.1	3.1	n.m.				
Ha 9-1C	60	2-phase L-V aqueous	Calcite cement	83.3	0.5							
Ha 9-1D	61b	2-phase L-V oil	Calcitized bioclast	122	2							
Ha 9-1D	62	2-phase L-V oil	Calcitized bioclast	48.9	1							
Ha 9-1D	63	2-phase L-V aqueous	Calcitized bioclast	79.5	0.5							
Ha 9-1D	64	2-phase L-V aqueous	Calcitized bioclast	80.9	1							
Ha 9-1D	65	2-phase L-V aqueous	Calcitized bioclast	82.9	1							
Ha 9-1D	67	2-phase L-V aqueous	Calcitized bioclast	79.6	1							
Ha 9-2A	1	2-phase L-V aqueous	Calcitized bioclast	90.6	0.5							
Ha 9-2A	2	2-phase L-V aqueous	Calcite cement	76.1	0.5							
Ha 9-2A	3	2-phase L-V aqueous	Calcite cement	102.3	1							
Ha 9-2A	7	2-phase L-V aqueous	Calcite cement	75.4	1							
Ha 9-2A	8	2-phase L-V aqueous	Calcite cement	74	0.3							
Ha 9-4A	10	2-phase L-	Calcite	77.3	0.3							



Table 4. Synopsis of the Re-Os isotopic data of asphaltene fractions from oil from the Halahatang oilfield, Tarim basin, China.

Sample	Re (ppb)	±	Os (ppt)	±	<sup>192</sup> Os (ppt)	±	<sup>187</sup> Re/ <sup>188</sup> Os	±	<sup>187</sup> Os/ <sup>188</sup> Os	±	rho	*Os <sub>285Ma</sub>
<b>Ha 9</b>	0.81	0.01	37.4	0.4	12.9	0.2	125.4	2.8	1.66	0.04	0.723	1.06
<b>Ha 9rpt</b>	1.23	0.02	57.2	0.7	19.5	0.4	125.2	3.2	1.74	0.04	0.732	1.14
<b>Ha11</b>	0.56	0.02	12.1	0.5	3.9	0.4	283.3	30.4	2.30	0.24	0.920	0.95
<b>Ha701</b>	0.07	0.01	4.9	0.3	1.7	0.2	78.7	16.0	1.48	0.19	0.612	1.11
<b>XK4-3</b>	0.85	0.02	8.8	0.6	2.3	0.5	736.8	147.9	4.68	0.93	0.989	1.17
<b>Ha15-2</b>	9.47	0.03	35.2	0.5	11.4	0.3	1655.2	39.7	2.25	0.05	0.970	-5.63
<b>Ha15-2rpt</b>	5.86	0.02	22.0	0.4	7.1	0.3	1636.7	59.9	2.25	0.08	0.983	-5.54

\*Os<sub>285Ma</sub> = <sup>187</sup>Os/<sup>188</sup>Os measured calculated at the time of oil generation (258 Ma) to yield the initial <sup>187</sup>Os/<sup>188</sup>Os composition.